OXIDE CERAMIC LASER

Charles D. Greskovich

General Electric Corporate Research and Development

Prepared for:

Office of Naval Research
Advanced Research Projects Agency

24 July 1973

GENERAL ELECTRIC

GENERAL ELECTRIC COMPANY
CORPORATE RESEARCH AND DEVELOPMENT
Schenectady, N.Y.

OXIDE CERAMIC LASER

FINAL TECHNICAL REPORT (ITEM 0002-A003)

Program Code No.: 02D10K71

Contract No.: N00014-70-C-0360

Principal Investigator: Charles D. Greskovich
(518) 346-8771
Ext. 6122

Contractor: General Electric Company
Corporate Research and Development

Effective Date: June 1, 1970

Expiration Date: May 31, 1973

Amount of Contract: $297,398.00

July 24, 1973

Scientific Officer: A. M. Diness, Code 471
Office of Naval Research
Arlington, Va. 22217

Sponsored by

Advanced Research Projects Agency
ARPA Order No. 1587, Amend. #3

The views and conclusions contained in this document are those of the author and should not be interpreted as necessarily representing the official policies, either expressed or implied, of the Advanced Research Projects Agency of the U. S. Government.

This research was supported by the Advanced Research Projects Agency of the Department of Defense and was monitored by ONR under Contract No. N00014-70-C-0360.

SRD-73-108

UNCLASSIFIED

Security Classification

DOCUMENT CONTROL DATA - R & D

(Security classification of title, body of abstract and indexing annotation must be entered when the overall report is classified)

1. ORIGINATING ACTIVITY (Corporate author)
General Electric Company
Corporate Research & Development
Post Office Box 8
Schenectady, New York 12301

2a. REPORT SECURITY CLASSIFICATION
Unclassified

2b. GROUP

3. REPORT TITLE

OXIDE CERAMIC LASER

4. DESCRIPTIVE NOTES (Type of report and inclusive dates)
Final Technical Report, June 1, 1970, through May 31, 1973

5. AUTHOR(S) (First name, middle initial, last name)

Charles D. Greskovich

6. REPORT DATE	7a. TOTAL NO. OF PAGES	7b. NO. OF REFS
July 24, 1973	87 100	29

8a. CONTRACT OR GRANT NO.	9a. ORIGINATOR'S REPORT NUMBER(S)
N00014-70-C-0360	
b. PROJECT NO.	SRD-73-108
c. ARPA Order #1587 Amend. #3	9b. OTHER REPORT NO(S) (Any other numbers that may be assigned this report)
d. O2D10K71	

10. DISTRIBUTION STATEMENT

11. SUPPLEMENTARY NOTES	12. SPONSORING MILITARY ACTIVITY
Details of illustrations in this document may be better studied on microfiche	Advanced Research Projects Agency 1400 Wilson Boulevard Arlington, Virginia 22209

13. ABSTRACT

Polycrystalline ceramic laser rods, composed of a cubic solid solution of 89-94 mole % Y_2O_3, 10-5% ThO_2 and 1% Nd_2O_3, were synthesized by a conventional ceramic sintering approach. Rods of this material, called Nd-doped Yttralox (NDY) ceramic, can be produced with threshold energies lower than that of the best commercially available Nd:glass laser and with a lasing efficiency ~93% that of laser glass at 40J of input energy under pulsed mode conditions. Laser rods can be produced with large variable intermediate-gains by controlled composition; lasing efficiencies depend strongly on cooling rate from the sintering temperature and on the method of powder preparation and processing. Preliminary measurements of laser induced damage in NDY ceramic reveals that surface damage preceeds bulk damage and that these damage thresholds are presently about 1/4 that of laser glass.

Active attenuation coefficients for AR-coated NDY laser rods are about 2% cm^{-1} as compared to 0.76% cm^{-1} for an OI ED-2 laser glass rod measured in the same optical cavity. The absorption component of the optical attenuation is 0.38% cm^{-1} at $\lambda = 1.064$ μm, indicating that the scattering component is the major contribution to the attenuation coefficient.

Careful powder preparation and processing procedures and controlled oxidation of Yttralox ceramic can generate a visible-middle infrared filter or an infrared filter with porosities as low as 10^{-6} to 10^{-7}.

DD FORM 1 NOV 65 1473

UNCLASSIFIED

Security Classification

14 KEY WORDS	LINK A		LINK B		LINK C	
	ROLE	WT	ROLE	WT	ROLE	WT
Nd-doped Yttralox lasers						
Laser Threshold and Efficiency						
Laser-induced Damage Threshold						
Ceramic Processing						
Sintering						
Grain Growth						
Pores						
Spectral Transmittance						
Scattering Centers						

- TABLE OF CONTENTS -

FOREWORD

This research was sponsored by Advanced Research Projects Agency and carried out in the Metallurgy and Ceramics Laboratory and the General Physics Laboratory of the General Electric Company Corporate Research and Development under U.S. Navy Contract N00014-70-C-0360 entitled "Oxide Ceramic Laser".

This work was administered under the direction of Dr. Arthur Diness from June 1, 1971, to May 31, 1973.

The author acknowledges the contributions of the following individuals to the Program:

- J. E. Burke and R. J. Charles for helpful guidance during this program:
- J. C. Almasi and J. P. Chernoch for many active and passive optical measurements:
- A. Feldman for laser induced damage of Nd-doped Yttralox under passive testing.
- C. O'Clair, for ceramic processing procedures and heat treatments:
- W. L. Roth for thoughtful consultation.
- M. K. Chun for active Q-switching measurements.

- ABSTRACT -

Polycrystalline ceramic laser rods, composed of a cubic solid solution of 89 - 94 mole % Y_2O_3, 10 - 5% ThO_2 and 1% Nd_2O_3, were synthesized by a conventional ceramic sintering approach. Rods of this material, called Nd-doped Yttralox (NDY) ceramic, can be produced with threshold energies lower than that of the best commercially available Nd:glass laser and with a lasing efficiency ~93% that of laser glass at 40J of input energy under pulsed mode conditions. Laser rods can be produced with large variable intermediate-gains by controlled composition; lasing efficiencies depend strongly on cooling rate from the sintering temperature and on the method of powder preparation and processing. Preliminary measurements of laser induced damage in NDY ceramic reveals that surface damage preceeds bulk damage and that these damage thresholds are presently about 1/4 that of laser glass.

Active attenuation coefficients for AR-coated NDY laser rods are about 2% cm^{-1} as compared to 0.76% cm^{-1} for an OI ED-2 laser glass rod measured in the same optical cavity. The absorption component of the optical attenuation is 0.38% cm^{-1} at λ = 1.064 μm, indicating that the scattering component is the major contribution to the attenuation coefficient.

Careful powder preparation and processing procedures and controlled oxidation of Yttralox ceramic can generate a visible-middle infrared filter or an infrared filter with porosities as low as 10^{-6} to 10^{-7}.

- LIST OF ILLUSTRATIONS -

List of Illustrations (continued)

List of Illustrations (continued)

List of Illustrations (continued)

List of Illustrations (continued)

- LIST OF TABLES -

I. INTRODUCTION

Yttralox® ceramic is a polycrystalline material invented at General Electric Corporate Research and Development in 1964. This oxide ceramic has the C-type rare earth structure and is composed of a solid solution of approximately 90 mole % Y_2O_3 and 10% ThO_2 or ZrO_2. The molecular formula may be written as $Y_{1.89}\ Th_{0.11}\ O_{3.05}$, where the introduction of Th^{4+} ions is accomodated by the formation of oxygen interstitials for charge balance.[1] The ThO_2 or ZrO_2 acts as a sintering aid which not only reduces the normal rate of grain growth but also retards discontinuous grain growth during densification, permitting the attainment of a nearly pore-free ceramic body.[2] Spectral transmittance of Yttralox ceramic reveals that there is high transmittance between 0.25 and 9.5 μm with over 95% transmittance between 0.75 and 6 μm. Yttralox ceramic has the potential of being an efficient light transmitter or light generator (when appropriately doped), provided that it can be produced with low optical absorption and scattering.

A high optical quality polycrystalline ceramic, which has potential use as a laser host or a high power infrared window, should be an optically isotropic single phase of homogeneous composition, should have high purity and high thermal conductivity, and have high transparency (low optical loss) in the desired wavelength region of the electromagnetic spectrum. In polycrystalline substances with low optical absorption, scattering may appreciably attenuate the transmitted beam and is a most important difficulty. Scattering mechanisms are those which cause radiation to undergo a change in the direction of propagation. Sources of light scattering centers in polycrystalline ceramics are pores, solid second phases, compositional gradients within a single phase, grain boundaries and other lattice imperfections creating local modifications in refrac-

tive index.

The processing of ceramics completely free from pores and secondary phases is a long-standing technological objective to which much effort has been devoted over the last two decades. Although many of the physical and mechanical properties of various ceramic materials could be enhanced by achieving a state of theoretical density and phase purity, only a few ceramics have been produced that closely approach this state. Lucalox® and Yttralox® ceramics, the IRTRAN series of hot pressed materials[3] and hot pressed PLZT ferroelectrics[4] are in this category. Preliminary investigations showed that with the sintering technology known three years ago, Yttralox ceramic had the potential of being synthesized with extraordinary optical perfection by a cold pressing and sintering approach. It is believed that this approach has the following advantages over hot pressing: Material can be produced with (1) better optical quality, (2) larger sizes and complex shapes and (3) the absence of insoluble gas-filled pores in the microstructure.

At the beginning of this research and development program (June, 1970) directed towards developing and evaluating Nd-doped Yttralox ceramic as lasers, the state-of-the-art powder preparation and processing yeilded sintered material with about 10^{-4} porosity, occasional solid second phases, and other optical distortions. The first method of powder preparation and processing involved mixing of the commercially available pure oxide components in a colloid mill and, after powder compaction, heat treating this mixture at high temperature to complete the solid-state reaction. A second method was a modified wet-chemical method which involved mixing commercially available pure Y_2O_3 powder with a thorium (or zirconium) salt and calcining to decompose the homogeneously distributed salts. After

grinding the screening the calcined powder, this mass is isostatically pressed into shape and fired at 2100°C to produce a dense ceramic. Fluorescent dopants were usually added to the batch in oxide form at one of several of the processing steps. Deviations from optical perfection noted in Yttralox ceramic produced by both methods were believed to have originated from irregularities such as powder agglomerates and impurity particles in the commercially available powders. It was believed that these problems could be overcome by working under higher purity conditions, and in particular, by using powders made in our own laboratory instead of commercial powders.

If Nd-doped Yttralox (NDY) ceramic can be produced with excellent optical quality by improved powder preparation and processing techniques, this polycrystalline ceramic would be attractive as an intermediate gain laser because it has a fluorescent emission linewidth (~73Å) between that (~7Å) of Nd:YAG[5] and that (~260Å) of Nd:glass[6]. Using conventional rod design with optical pumping methods, neither Nd:YAG or Nd:glass provide the desirable dual capability of high peak and high average power output because Nd:YAG has an intrinsic inability to achieve very large population inversion of electrons necessary for high peak power, whereas Nd:glass has a low thermal conductivity (~10mW/cm°C)[7] which restricts high average power output. NDY ceramic may meet these dual characteristics because it has a broader fluorescent emission linewidth than that of Nd:YAG and a thermal conductivity about 6 times that of Nd:glass. The use of Nd^{3+} as a fluorescent center in the Yttralox laser host has the principal advantage of providing a low threshold for stimulated emission at 1.074 μm and places a premium on the optical perfection of the host and low optical cavity loss.

II. PROGRAM GOALS

The ultimate goal of this research program is to produce an efficient, intermediate gain NDY laser which emits at 1.074 μm or a high-power infrared window material for the 1 to 6 μm wavelength region. In striving to attain this goal, major effort was devoted towards generating and understanding the origin of optical defects or inhomogeneities and ways to eliminate or minimize them in sintered ceramics.

The overall objectives, then, are to:

(1) Develop a powder preparation and processing technique to reproducibly fabricate ultra-clear NDY ceramic comprised of 89 mole % Y_2O_3, 10% ThO_2 and 1% Nd_2O_3 or of a more suitable composition;

(2) understand the origin of pores, solid second phases, and other light-scattering defects, the mechanisms of their removal, and the methods to determine their concentration, shpae and size distribution in laser-quality material;

(3) understand the interrelationships between powder preparation and processing, microstructural development and optical quality of the sintered product;

(4) evaluate NDY ceramic as a potentially efficient, intermediate gain laser under both pulsed mode and Q-switching conditions and determine the damage threshold characteristics of NDY lasers under both active and passive conditions.

III. MAJOR ACCOMPLISHMENTS

Since the text is extensively detailed in a variety of areas in both ceramic science and optical physics, the major findings of this research and development program are listed in this section for convenience sake to the reader.

(1) NDY laser rods (3" x 1/4") could by synthesized with threshold energies lower than that of a commercially-available Nd:glass laser (Owens-Illinois, Ed-2) and with a lasing efficiency ~93% that of laser glass at 40J of input energy under identical pulsed mode conditions.

(2) NDY laser rods can be produced as a controlled intermediate gain laser because the fluorescent linewidth of the Nd^{3+} ions at the lasing transition increases linearly with increasing ThO_2 content in the Y_2O_3 structure.

(3) A large increase in lasing efficiency was found for NDY rods rapidly-cooled rather than slowly-cooled from the sintering temperature of 2170°C and is related probably to nucleation and growth of submicroscopic scattering centers having compositional variations in the solid-solution matrix.

(4) Preliminary laser-induced damage threshold measurements, performed on NDY laser rods in both the active and passive modes, show that surface damage preceeds bulk damage and that these damage thresholds are about 1/4 that of laser glass with good optical quality.

(5) The absorption component of the optical attenuation component in NDY rods was measured by a precision calorimetric technique and determined to be 3.8×10^{-3} cm^{-1} at $\lambda = 1.064$ μm, a value which is only 27% of the total optical loss. Hence, the scattering component is responsible for most light attenuation in these ceramic lasers.

(6) Reproducible fabrication of laser-quality NDY material can be achieved by using an oxalate powder approach combined with a ball-milling operation.

(7) Porosities as low as 10^{-6} to 10^{-7} are attained in NDY ceramics, provided that the number densities of large pores and pore clusters are low.

(8) A comparative analysis shows that Yttralox ceramic exhibits superior spectral transmittance characteristics in the visible and middle infrared region than hot-pressed spinel, MgO and ZnSe.

(9) Controlled oxidation of Yttralox ceramic can generate a visible-middle infrared filter or just an infrared filter.

IV. POWDER PREPARATION, CERAMIC PROCESSING AND HEAT TREATMENT

Two basic methods of powder preparation, processing and heat treatment developed simultaneously to improve the optical perfection of sintered Y_2O_3 containing 10 mole % ThO_2 and 1% Nd_2O_3 in solid solution were the "sulfate" and the "oxalate" processes.[8] Ten mole % ThO_2 was chosen to insure effective grain growth inhibition but the ThO_2 content was varied from 2.5 to 10 mole % in the oxalate process. Considerable effort was made to improve the sulfate process during the first year's contract because this process generated the first NDY laser rod. Although transparent material could be produced by the sulfate method, several impurities were discovered during the first year and, as a result, this process was discontinued. The sulfate process is only described in the following section, and there will be no further discussion of this process later in the text.

A. Sulfate Process

Yttrium oxide powders from five commercial sources were examined during the course of this investigation. Although the commercially designated purity (~99.99%) of these powders was specified in terms of total rare earth impurities, all powders frequently contained nonwhite impurity particles. Spectrochemical and X-ray diffraction analyses of these impurity particles, which were collected by a screening technique, showed high levels of Al, Si, Fe_2O_3 and ZnO. One powder* was selected for further work because it had relatively high purity and a narrow particle size distribution. From the cumulative particle size distribution measured with a Coulter counter, the average particle size was determined to be about 3 μm. The particle size ranged between approximately 10 μm and less than 0.8 μm.

The sulfate process consisted of adding an aqueous (deionized H_2O)

* Molybdenum Corporation of America, Louviers, Colorado

suspension of yttrium oxide powder into a filtered aqueous solution of thorium and neodymium sulfates. The purity of the sulfates was 99.9%. The batch composition was 89 mole % Y_2O_3, 10% ThO_2 and 1% Nd_2O_3. Methods utilized to intimately mix the Y_2O_3 particles in the sulfate solution were: magnetically stirring with a Teflon-coated stirring bar and mixing in a stainless steel, colloid mill. After colloid milling, the suspension was transferred to a glass beaker and magnetically stirred. While mixing vigorously, heat was applied so that the suspension dried as rapidly as possible without causing violent boiling or salt segregation. The resulting powder was dried for approximately 12 hours at 110°C in air and screened through a nylon screen (-100 mesh) to improve particle size and compositional uniformity. In order to convert the sulfates to oxides, the powder was calcined in open alumina boats for ~7 hours at 1000°C in flowing air (3SCFH).

The calcined powder was cold-pressed into pills ~1 inch in diameter and 3/16 inch high or pressed isostatically into rods ~3 inch in diameter and 4 1/2 inches long at 40,000 psi. Pressed samples, having relative green densities ~60% of theoretical, were then given a second calcination for 15 hours at 1350°C in flowing air to further remove residual sulfur from the calcined powder. Specimens were heated in about six hours to 2170°C, typically sintered for about 20 to 125 hours at 2170°C in dry H_2 (dew point ~-70°C), and finally cooled to room temperature in about six hours in wet hydrogen (dew point ~25°C).

The morphology and particle size of powder calcined for seven hours at 1000°C in air are shown in Fig. 1. The larger Y_2O_3 particles are ~3 μm in size and are coated with very small particles (~1000Å or less) of ThO_2 and, presumably, Nd_2O_3. This "coating" behavior enhances composition homoteneity and promotes inhibition of discontinuous grain growth.

Figure 1 SEM photomicrograph of calcined powder prepared by the sulfate process. 4300X

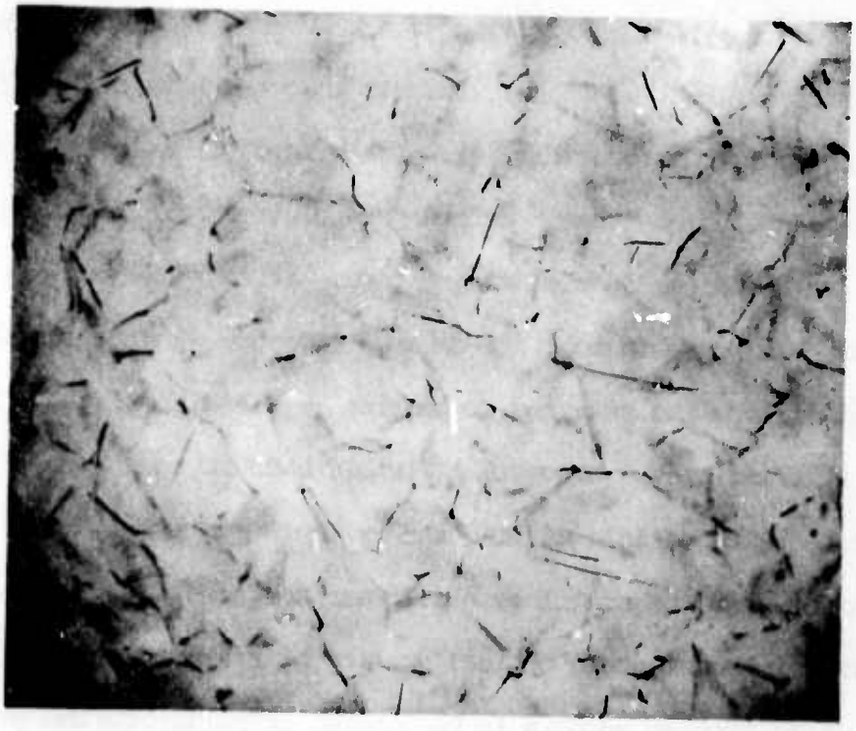

Figure 2 Grain-boundary phase in sintered material prepared by the sulfate process. Transmitted light. 185X

Sintered material of high optical quality could be produced from this powder, provided that a second calcination was given to the powder compacts and an extended sintering time was used at high temperatures. If a second calcination was omitted, specimens frequently deformed during sintering at 2170°C. Specimens sintered for less than ~30 hours contained an observable amount of second phase that wets the grain boundaries (Fig. 2). A sulfur Kα display obtained with the electron microprobe is shown in Fig. 3 and demonstrates that sulfur is concentrated in the grain-boundary phase. This second phase is removed much faster from the surface region of the sintered piece than from the specimen interior. In a 1/4-inch-thick specimen, this phase completely disappears by firing for times greater than 30 hours at 2170°C.

The removal of the grain boundary phase from sintered material makes possible the clear observation of a second optical defect, which is porosity. Although sintered specimens 1/4 inch thick are transparent to the unaided eye, transmitted light microscopy reveals that there is still a high density of pores and pore clusters (Fig. 4). The size of individual pores in a cluster is usually less than 5 μm and such clusters are found generally inside grains. Large, faceted-shaped pores having sizes between 20 and 50 μm (not shown) are found in most specimens. The pore density is markedly reduced by colloid milling the starting suspension (Y_2O_3-salt solution) rather than magnetic stirring only. However, a visible haze in the sintered material is associated with colloid milling and is caused primarily by Fe and Ni contamination from the stainless steel wear surfaces.

Further improvement in optical quality of sintered material produced by the sulfate process appears to be limited primarily by the purity of the starting Y_2O_3 powder and the metallic contamination introduced during colloid milling. The inability to eliminate large pores in the 20 to 50 μm

Figure 3 Electron probe, X-ray K_α display of sulfur in the grain-boundary phase. 1088X

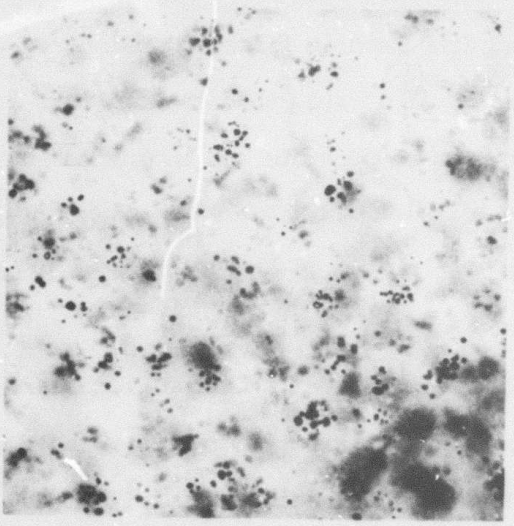

Figure 4 Porosity in sintered material prepared by the sulfate process. Transmitted light. 235X

range by changes in powder processing is thought to be associated with impurity particles in the Y_2O_3 powder. Iron and nickel contamination introduced by colloid milling will undoubtedly have an adverse effect on lasing behavior and other optical properties of the sintered product.

B. Oxalate Process

The oxalate process was developed to (1) eliminate foreign particles by filtering the starting solutions and maintain a high degree of cleanliness during the ensuing processing steps; (2) attempt to achieve a homogeneous distribution of Y^{3+}, Th^{4+}, and Nd^{3+} ions to ensure composition uniformity in the powder synthesized; (3) obtain a small average particle size to enhance the sintering rate; and (4) reduce the long heat treatment required for sulfur elimination from powders prepared by the sulfate process.

Yttrium, thorium, and neodymium nitrates were the starting raw materials which had purities of 99.99%, 99.9% and 99.999%, respectively. These nitrates were weighed in the correct proportions to produce NDY ceramics of variable Y_2O_3 and ThO_2 contents and dissolved in filtered, deionized water. This salt solution was filtered and dripped at a rate ~60 drops/min into a filtered oxalic bath which was 80% saturated at room temperature and contained 100% excess oxalic acid required to convert the nitrates into oxalates. The precipitation reaction may be written as $R(NO_3)_x + H_2(C_2O_4) \rightarrow R(C_2O_4)_y\downarrow + HNO_3$ where R represents yttrium, thorium and neodymium. During precipitation, the oxalic acid bath was continuously stirred with motor driven stirring propeller. After precipitation, the oxalate precipitate was stirred vigorously, washed with filtered deionized water to remove residual acid, vacuum filtered, dehydrated at 110°C for 24 hours, and calcined for four hours between 800° and 850°C in flowing air (3 SCFH).

The calcined powder was bluish-white in color and was either directly cold-pressed into shape, as described above, or dry-milled with 1 wt % stearic acid in a rubber-lined ball mill (volume = 1.2ℓ) that contained 10 mole % ThO_2-doped Y_2O_3 cylinders as a grinding medium. After ball milling for 6 hours, the powder was light yellow and smelled like "rubber". In order to remove stearic acid and rubber particles introduced in the powder during the milling operation, specimens formed isostatically at 30 Kpsi from milled powder were given an oxidizing treatment for 2 hours at 1100°C in air. Specimens were then sintered at high temperature in a similar manner as that described in the sulfate process.

Powder particles, synthesized by the oxalate method and having the nominal composition of 89 mole % Y_2O_3, 10% ThO_2 and 1% Nd_2O_3, were approximately parallelpipeds with a size range between 0.3 and 3 μm [Fig. 5(a)]. After calcination at 800°C for four hours, there was agglomerate formation and an observable morphological change of the original oxalate particles [Fig. 5(b)]. Debye-Scherrer photographs showed that the calcined powder consisted predominantly of a Y_2O_3 solid solution plus a trace of a thorium oxide phase. Particles of the calcined powder were composed of small crystallites of the order of 200Å in size (Fig. 6); this was also confirmed by electron diffraction. After ball-milling the calcined powder, particles were of the order of 0.1 μm [Fig. 5(c)]. The powder agglomerates in the ball-milled powder were quite fragile and broke up when lightly squeezed between microscope slides.

(a) 4400X

(b) 4400X

(c) 1000X

Figure 5 SEM photomicrographs of (a) powder particles synthesized by the oxalate process; (b) oxalate powder calcined for 4 hours at 800°C in air; and (c) ball-milled powder.

Figure 6 Transmission electron micrograph of a particle of oxalate powder calcined at 800°C for 4 hrs in air. 75000X

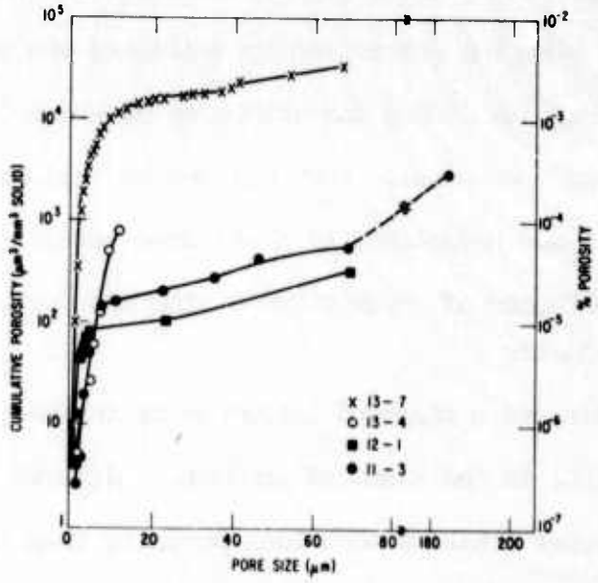

Figure 7 Cumulative porosity versus pore size for several NDY rods. Heat treatments are given in Table I.

V. MICROSTRUCTURAL CHARACTERIZATION OF YTTRALOX CERAMIC MADE BY THE OXALATE PROCESS

A. Porosity

1. Quantitative Determination of Porosity

The quantitative determination of the porosity in a polished, sintered specimen was easily accomplished with a petrographic microscope using a ruled graticule and transmitted white light. The technique involved (1) selecting three different magnifications at 30X, 80X and 460X; (2) scanning through known cylindrical volumes; (3) counting the number of pores and measuring their average size; and (4) recording only pores with an average pore size greater than 22μ at 30X, between 5μ and 22μ at 80X, and between 0.5μ and 5μ at 460X. There were relatively few pores smaller than 0.5 μm, as determined by ultramicroscopy (see later).

Pores less than 0.5μ could not be resolved at 460X. In general, the total number of pores counted was approximately 100 to 200. The solid volumes analyzed at 30X, 80X and 460X were approximately 900 mm^3, 30mm^3, and 3 mm^3, respectively. The average dimension of an occasional irregularly shaped pore was determined by averaging the maximum and minimum linear dimensions (excluding tubular pores of which only a few were observed in many specimens). Pore volumes in various size ranges were then calculated and normalized to a standard total scanned volume of solid.

2. Influence of Ceramic Processing and Composition on Residual Porosity

There is a profound influence of ceramic processing on residual porosity in the sintered product. Sintered material made from ball-milled powder contains much less porosity than that derived from unmilled powder. Cumulative porosity versus pore size is plotted semilogarithmically in Fig. 7 for several NDY rods of good optical quality. The

total or residual porosity for each rod is given by the terminus of its respective curve in Fig. 7 and is also listed in Table I along with the corresponding heat treatment. Cumulative porosity and pore density as a function of pore size found typically in sintered material produced from unmilled powder (specimen 13-7) are shown in Figs. 7 and 8, respectively. The other data plotted in Fig. 7 were obtained from sintered specimens synthesized from ball-milled powder; pore density versus pore size for specimen 12-1 is shown in Fig. 9. A comparison of these data for specimens 13-7 and 12-1 shows that the ball-milling procedure reduced residual porosity and pore density by 1 to 2 orders of magnitude over the same pore size range. Furthermore, for the ceramic processing steps utilized, the pore size distribution peaked between 1 and 2 μm with most pores between 0.5 and 5 μm in size. As will be shown later, about 20% of the pores are less than 0.5 μm in size, and these pores only slightly modify the above general observations. It has been suggested[8] that the ball-milling operation enhanced dispersion of the ThO_2 grain-growth inhibitor in the calcined powder which permitted a greater majority of pores to remain on grain boundaries for a longer period of time and thus shrink during densification.

TABLE I

Heat Treatment and Porosity in NDY Rods Containing 10 mole % ThO

Sample	Sintering time at 2170°C (hr)	Porosity
11-3	58	3.2×10^{-6}
12-1	125	3.3×10^{-7}
13-4	80	8.2×10^{-7}
13-7	92	3.5×10^{-5}

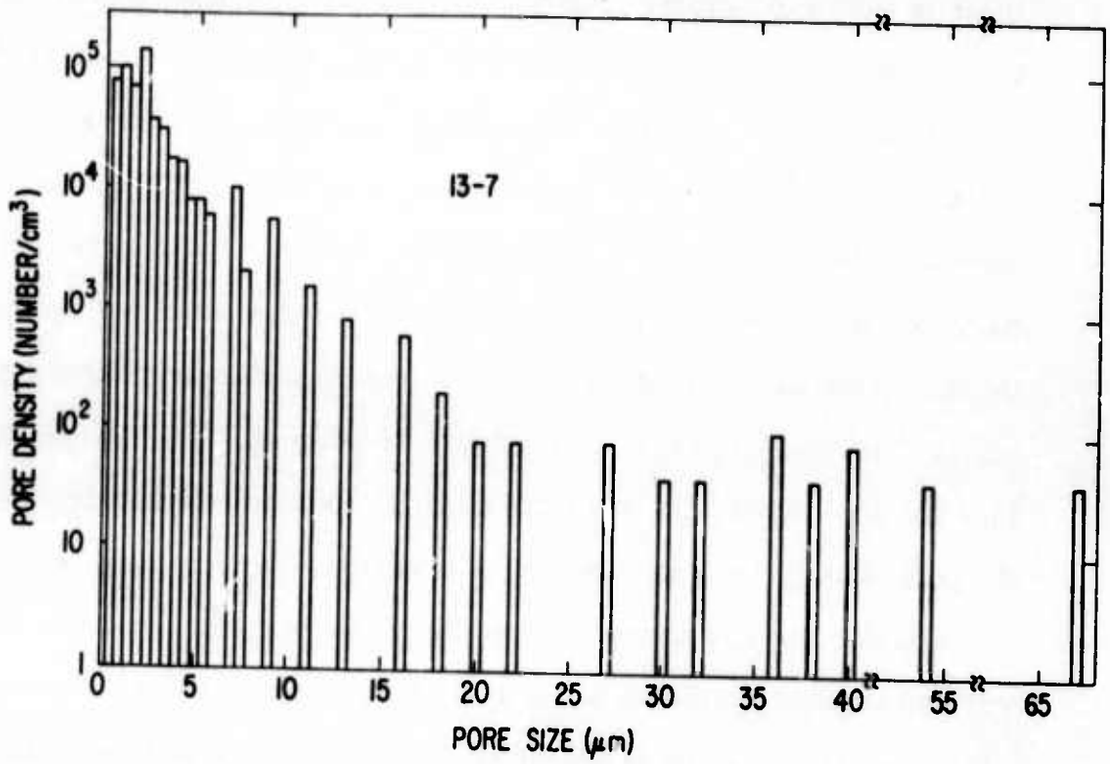

Figure 8 Pore density versus pore size in NDY rod 13-7 prepared from unmilled powder.

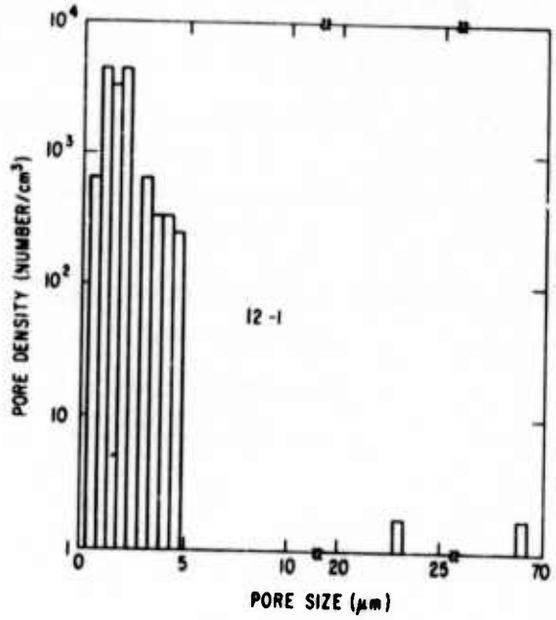

Figure 9 Pore density versus pore size in NDY rod 12-1 prepared from ball-milled powder.

The oxalate precipitation approach combined with the ball-milling operation also produced low porosity, sintered material having variable ThO_2 and Y_2O_3 contents. The compositions investigated were 2.5, 5 and 10 mole % ThO_2, with Nd_2O_3 content fixed at 1 mole %. NDY ceramics which contained 2.5 and 5 mole % ThO_2 and were processed and heat treated under identical conditions as specimen 12-1 (which contains 10 mole % ThO_2) had similar pore size distribution curves as that of 12-1 except for the absolute magnitudes of pore densities. The pore size distribution found in a specimen containing 2.5 mole % ThO_2 is given in Fig. 10. Although the number density of pores in the 1 to 2 μm range was approximately 100 times higher than that found in 12-1, the porosity (5×10^{-6}) was higher by only a factor of 15 because the volume fraction porosity depends on the cube of the average pore size, and is small for micron size pores. For the case of NDY ceramics containing 5 mole % ThO_2, the number density of pores was only slightly higher than that for the 10 mole % ThO_2 material and corresponded to a residual porosity of 1.1×10^{-6} which is about a factor of 3 higher.

An average pore size of 1 to 2 μm generally found in all sintered NDY material implies that pore growth has occurred during densification. Since the powder compacts made from milled powder consist of particles of the order of 0.1 μm in size and have a relative green density of 60% of theoretical, and since the coordination number of a given particle is about 6,[9] the average initial pore size must not be much larger than 0.1 μm. This suggests that the average pore size and corresponding pore size distribution shift to larger pore sizes during the sintering process. The mechanism of pore growth and the densification stage at which it takes place in sintered NDY ceramics have not been established. However, it has been reported that during the final stages of sintering of UO_2[10] pores can grow by pore coalescence if pores migrate with grain boundaries, and that pore

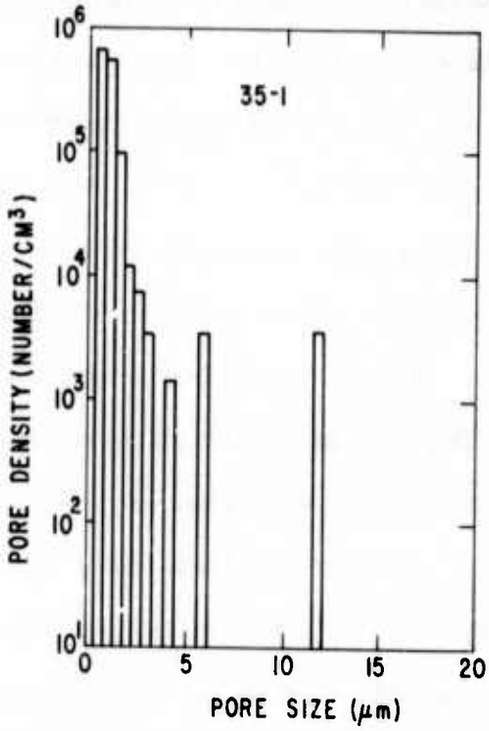

Figure 10 Pore density versus pore size in NDY rod 35-1 containing 2.5 mole % ThO_2.

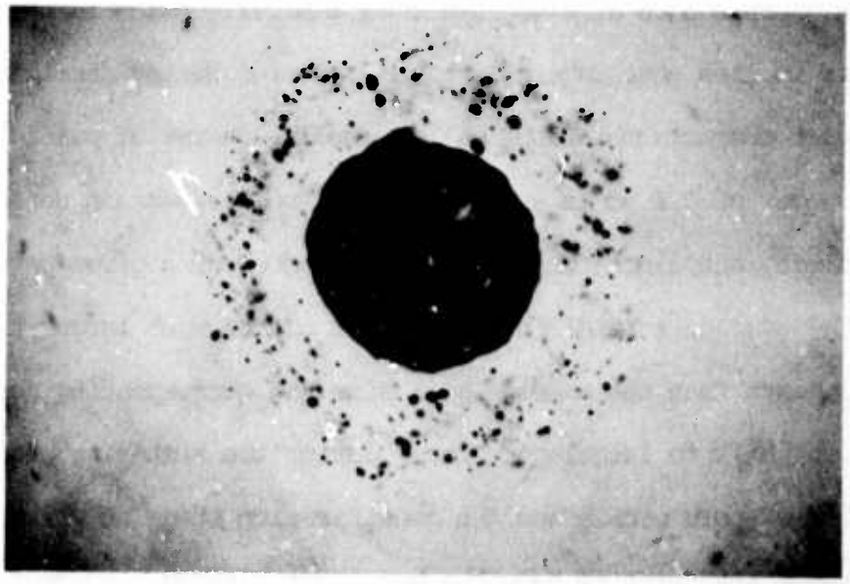

Figure 11 Galaxy of small pores stabilized in the vicinity of a large pore. Transmitted light. 158X

growth can also occur in metallic and nonmetallic materials[11,12] during the early and intermediate stages of sintering.

3. Large Pores

Sintered NDY ceramic prepared from either "as calcined" powder or from ball-milled powder contains, in general, an occasional large pore greater than 50 μ in size. Such large pores contribute greatly to light scattering losses because for pores much larger than the wavelength, the total scattering cross-section is equal to twice its geometrical cross section, $2\pi r^2$. In addition, large pores have small average curvatures and low driving forces for shrinkage. The elimination of these large pores is virtually impossible under practical conditions of isothermal sintering.

A large pore occasionally found in sintered material prepared from unmilled, calcined powder is shown in Figure 11. A galaxy of small pores surround the large one. In order to determine if the origin of these pores are caused by incomplete decomposition of the starting oxalate powder at 800°C for 4 hours in air, the calcination temperature was increased to 850°C. Sintered specimens prepared from this powder contained fewer large pores greater than 50μ in size. Apparently, the higher calcination temperature more completely decomposes the Y-Th-Nd oxalate to the respective oxides and minimizes the formation of these pores originating from a region that contained incompletely decomposed material.

The morphology and size of large pores found in sintered material prepared from ball-milled powder appears to depend on the type of mill lining. Typical photomicrographs of large pores found in sintered material

prepared from powder milled for 6 hours in rubber-lined and polyurethane-lined mills are shown in Figures 12 and 13, respectively. Most of these large pores are located at grain boundaries. In several instances, a particle of rubber or polyurethane in milled powders has been observed with the naked eye. The tubular-shaped pores illustrated in Figure 3 originate most likely from excessive abrasion of the polyurethane lining. Further support for the above conclusion can be deduced from preliminary milling experiments in which the surface roughness of the grinding medium was changed for the same weight of medium. Results show that the use of rough cylinders gives rise to a higher density of large pores in the sintered product, indicating a higher coefficient of friction between the rough cylinders and the mill lining.

4. Pore Clusters

During the second year of this contract, sintered NDY specimens prepared from ball-milled powder contained an unusually large number of pore clusters that were distributed randomly throughout the bulk of the material. Prior to this time, sintered material contained very few pore clusters when prepared by the identical process. Transmitted-light photomicrographs of various pore clusters are shown in Figure 14. Individual pores in a cluster were approximately 5μ or less in size and varied in number. In a few cases, over 100 pores have been observed in a given pore cluster. A typical pore cluster density commonly observed was approximately $30/mm^3$.

An extensive investigation of the origin of pore cluster formation in sintered NDY ceramics containing 10 mole % ThO_2 was obviously in order, especially since, from the author's experience, such pore clusters are frequently found in other polycrystalline ceramics with high optical quality, such as MgO-doped Al_2O_3 and Y_2O_3-doped ThO_2. This study

Figure 12 Large pore in sintered material prepared from ball-milled powder. Sintered 60 hours at 2170°C. Transmitted light. 270X

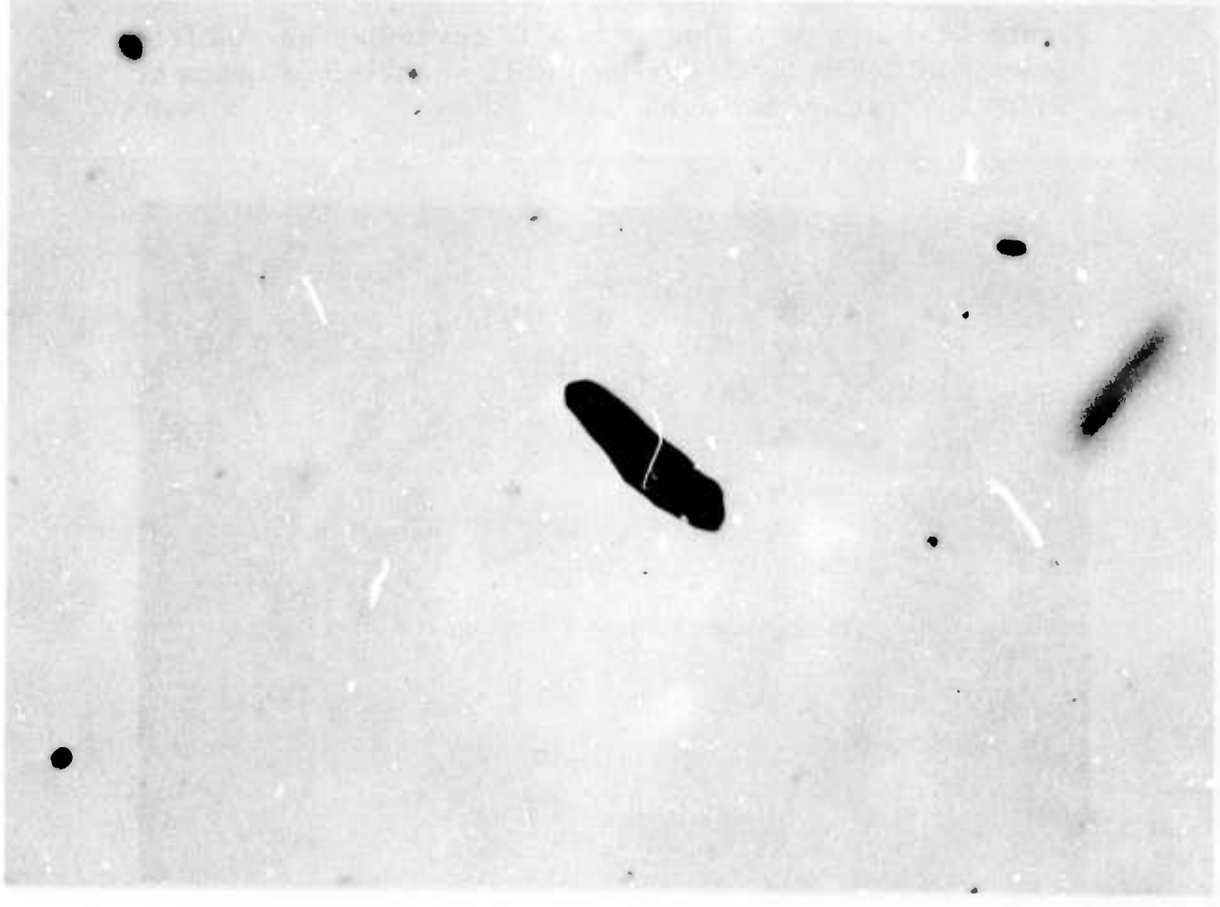

Figure 13 Large tubular-shaped pore in sintered material prepared from powder milled in a polyurethane-lined mill. Sintered 60 hours at 2170°C. Transmitted light. 240X

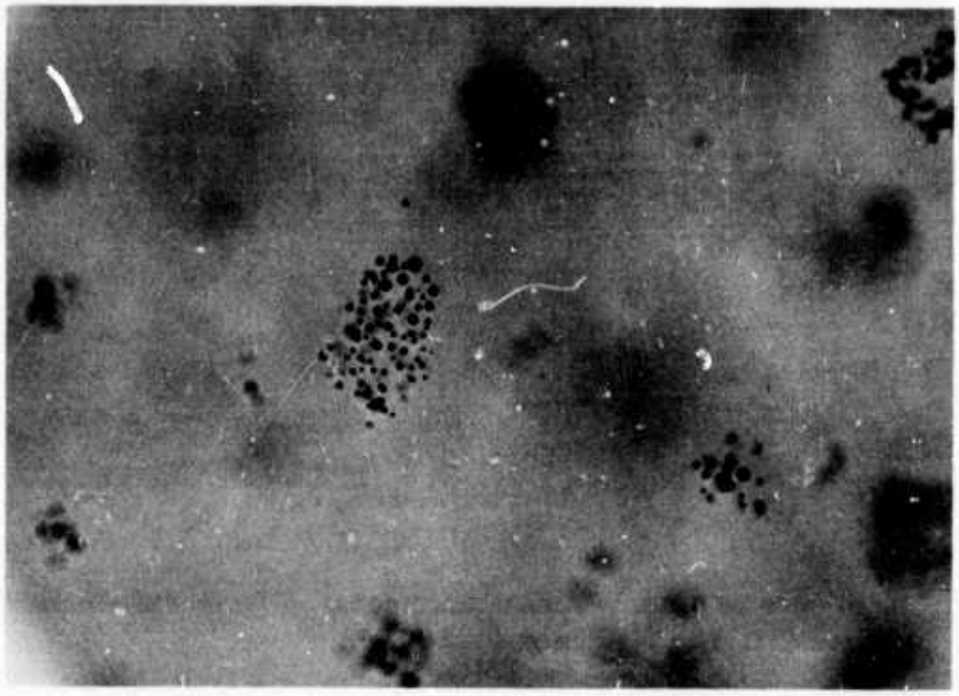

Figure 14 Large pore cluster in NDY ceramic prepared from powder milled in a rubber-lined mill. Sintered 34 hours at 2170°C. Transmitted light. 468X

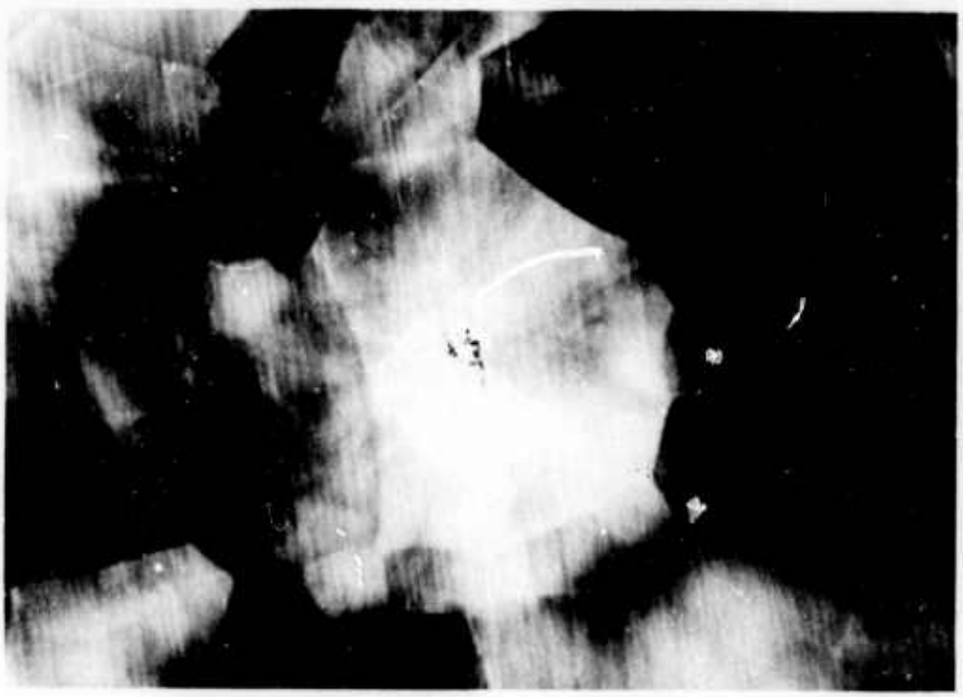

Figure 15 Pore cluster located inside a large grain having 11 sides (in cross-section). Grain boundaries revealed by surface grain birefringence caused by rough polishing. Polarized light. 187X

resulted in the following experimental findings:

(1) Sintered material made from unmilled, calcined powder contained very few pore clusters whereas that made from dry-milled, calcined powder always contained numerous pore clusters.

(2) Changing the weight ratio of grinding medium to powder charge in the rubber-lined mill from 24:1 to 20:1 had no major effect on cluster formation.

(3) The dry-milling of NDY powder with 1 wt % stearic acid in rubber-lined, neoprene-lined and polyurethane-lined mills yielded sintered material having many pore clusters.

(4) The dry-milling of NDY powder in the absence of stearic acid and the dry-milling of neodymium-free Yttralox powder also yielded material characterized by pore cluster formation.

(5) Pore clusters did not originate from contamination caused by the furnace atmosphere prevailing during the oxidation treatment at 1100°C, a processing step used only for compacts prepared from milled powder.

It was clear from these experimental observations that pore cluster formation originated during the ball-milling operation and that their elimination was not influenced by the weight ratio of grinding medium to powder charge, different ball-mill linings, absence of stearic acid, furnace atmosphere present during the oxidation step, and presence of the neodymium additive.

A close examination of the Yttralox cylinders used for the ball-milling experiments revealed that excessive wear occurred at various locations

on their surfaces. This was an indication that large chips had fragmented off of the cylinders during milling, mixed into the fine powder (0.1μ) batch, and acted as nuclei for discontinuous grain growth during sintering. Large chips are possible because the average grain size of the cylinders was approximately 100μ. By removing the most severely abraded cylinders by visual inspection and proceeding with a typical milling experiment, the number of pore clusters in the sintered material was drastically reduced to about 2 per mm^3 of solid. After a fire polishing treatment at high temperature, the use of the same cylinders during milling also produced sintered material essentially free of pore clusters. There was a tremendous increase in the number of pore clusters by roughening the surfaces of the fire-polished cylinders by first wet-grinding and then subsequently using these cylinders in a typical dry-milling experiment.

Two additional experiments were performed to establish, unequivocally, the origin of pore clusters in NDY ceramics. Fine grain sized (~1.5μ) Yttralox cylinders, containing 10 mole % ThO_2, were synthesized to increase the fracture strength of the cylinders and eliminate the source of large-size chips or fragments. The use of these fine-grained cylinders in the standard dry-milling step resulted in sintered material that contained less than 1 pore cluster per mm^3 of solid analyzed. If pore clusters were indeed caused by fragments much larger than the powder particles, then the intentional addition of coarse particles into the mill charge should cause the return of pore clusters in the sintered material. The addition of 0.5 wt % of -40 mesh (~420μ) NDY particles to the mill charge did produce over 200 pore clusters per mm^3 of sintered material.

The consequence of a markedly mixed particle size in the starting powder gives rise to a condition for discontinuous grain growth during sintering of the powder compact. A large particle in a fine powder matrix is a site for a discontinuous grain growth nucleus. During the early stages of sintering, discontinuous grain growth occurs and the grain boundaries developed at the interfaces between the large and small grains move on across pores and reform on the other side. If this mechanism is operating, then pores should be entrapped inside the rapidly growing grains. That such is the case can be seen in transmitted light photomicrographs illustrated in Figs. 15 and 16. Although the use of polished sections and reflected light microscopy cannot, in general, reveal pore clusters in a sintered specimen containing a small cluster concentration, this technique can show clusters very clearly when there is a large concentration due to the intentional addition of coarse particles into the fine powder during the milling step (Fig. 17). On the other hand, transmitted light microscopy can reveal the morphology and location of small concentrations of pore clusters when used in combination with sintered specimens having surface grain anisotropy caused by rough polishing (Fig. 15) and specimens containing a sulfur-rich phase which decorates the grain boundaries (Fig. 16).

It has been demonstrated, then, that the origin and mechanism of pore cluster formation in NDY ceramics (and most likely in other ceramics sintered in the solid state) are caused by a very broad particle size distribution in the powder compact which gives rise to discontinuous grain growth. Large particles in the distribution can arise from the abrasion of large grain size cylinders or balls used for ball-milling the powder or from the normal spread in the size distribution obtained by the powder particles during powder

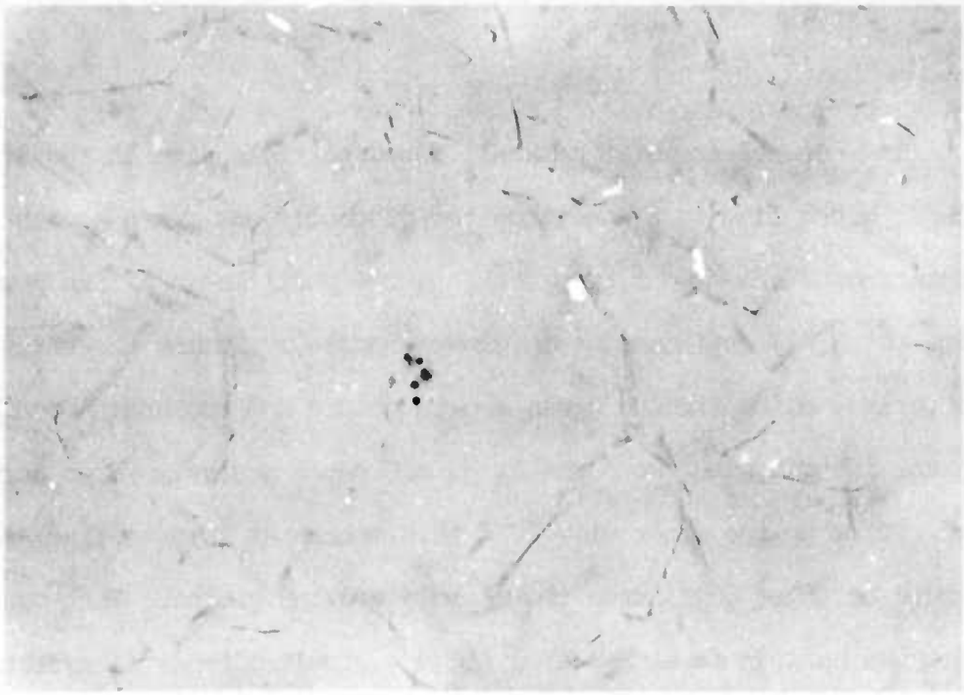

Figure 16 Pore cluster located inside a large grain whose boundaries are revealed by grain boundary decoration. Sintered 11 hours at 2115°C. Transmitted light. 187X

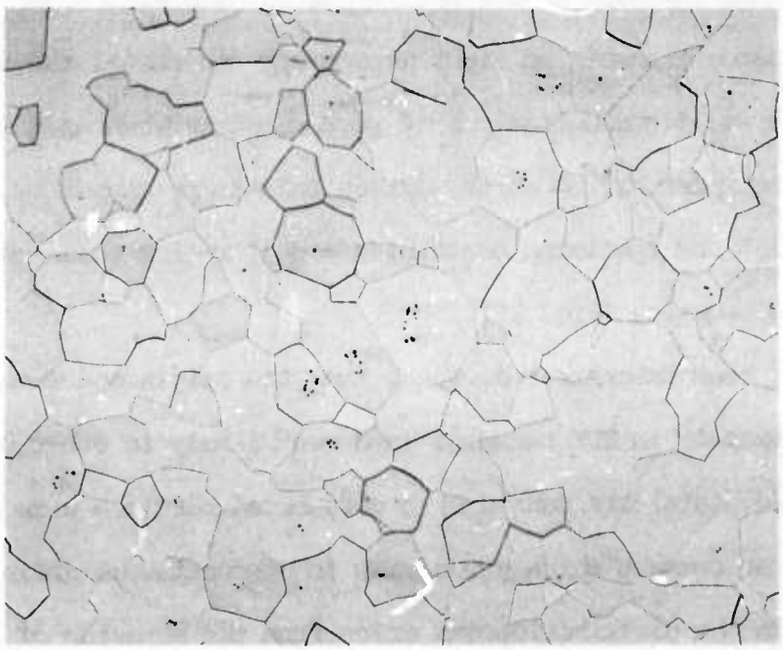

Figure 17 Pore clusters, having several morphologies, located inside grains. Sintered 16.5 hours at 2160°C. Reflected light. 87X

synthesis or milling. The elimination of pore cluster formation is essential to the production of sintered material with low porosity and high optical quality because, as stated above, pores shrink much more slowly when they are located off of, rather than on, grain boundaries. In the present case, the use of high purity, fine-grained (1.5μ) Yttralox cylinders for milling experiments has essentially eliminated pore clusters.

The pore size-frequency distribution measured in specimen 16-3 contains a majority of pore clusters (Fig. 18). This specimen was fabricated and sintered in the identical manner as specimen 12-1 (see Fig. 9). Note the tremendous increase in the number density of pores over the same pore size range when most pores are in the form of clusters. Specimen 16-3 had a relatively high porosity of 1.2×10^{-5} because it contained approximately 40 pore clusters per cubic millimeter of solid analyzed.

5. Kinetics of Grain Growth and Porosity Reduction During Final Stage Sintering.

Isothermal grain-growth measurements were made on compacts sintered for various times at 2000 and 2170°C in a dry hydrogen atmosphere (Fig. 19). For the same time and temperature, the average grain size was larger in sintered material prepared from powder milled in a rubber-lined mill than in sintered material prepared from unmilled powder. In addition, grain growth in specimens prepared from milled powder approximately followed a $t^{1/3}$ behavior whereas grain growth approximately followed a $t^{1/2}$ law for the unmilled material at 2000°C. These grain growth data in high-density, compacts with 1 to 9 mole % porosity can be understood by careful examination of the microstructure.

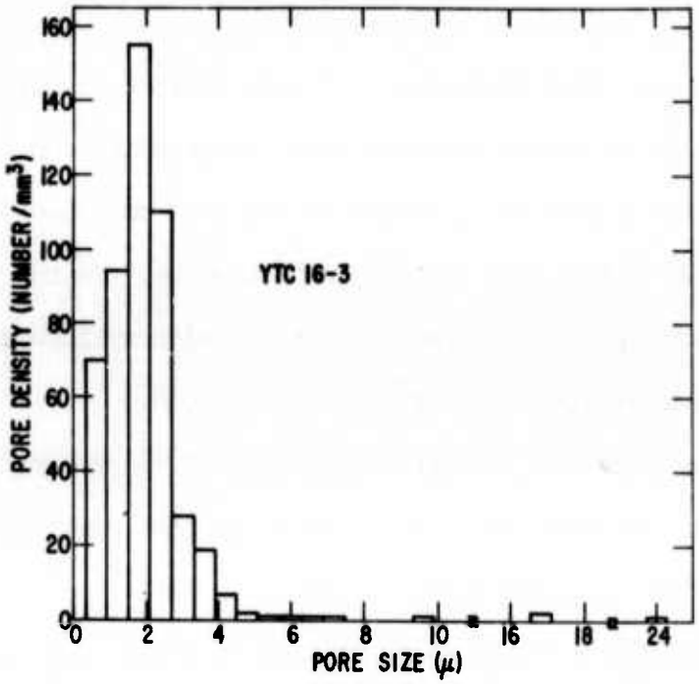

Figure 18 Pore density as a function of pore size for rod 16-3 in which most pores were in pore clusters.

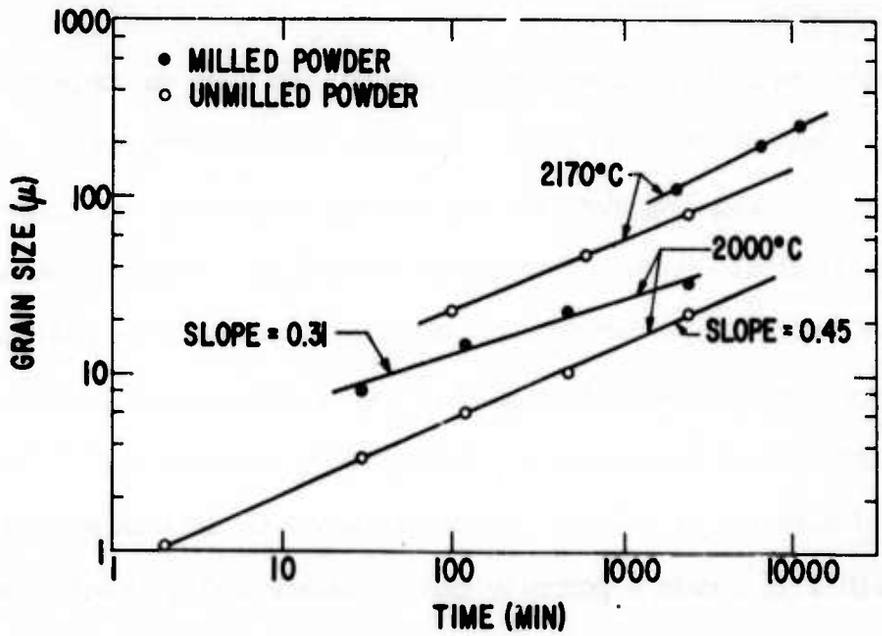

Figure 19 Grain size as a function of time and temperature for sintered NDY ceramic prepared from milled and unmilled powder.

The microstructure of a compact prepared from unmilled powder and sintered for two hours at 2000°C is shown in Figure 20. This sintered material is characterized by a cubic, single solid phase, as confirmed by X-ray diffraction, and a closed-pore phase distributed primarily at three and four grain intersections. The location of these pores are indicative of grain growth controlled by pore migration but the square grain-growth kinetics found experimentally are not in agreement with cubic kinetics predicted from theory[10]. Square grain-growth kinetics has been previously found[2] for Y_2O_3 containing various amounts of ThO_2 in solid solution. In that work, it was reasonably well demonstrated that the addition of ThO_2 to Y_2O_3 inhibits grain growth during sintering by the segregation of ThO_2 solute at grain boundaries, causing a decrease primarily in the grain boundary mobility. The major effect of the ThO_2 addition is to reduce grain-boundary mobility relative to that of pore mobility and thereby prevent pore entrapment during grain growth. It appears then, that the ThO_2 addition, not pores, is responsible for controlling grain growth such that a square growth law is observed at 2000°C and 2170°C. Square grain-growth kinetics has been theoretically proposed for the effect of impurity drag on grain-boundary migration during continuous or normal grain growth[13].

A typical grain structure developed during the sintering of NDY material made from ball-milled powder is shown in Fig. 21. In addition to the presence of pore clusters found inside grains, there was a highly-reflecting, solid second phase located at grain boundaries and grain intersections. A scanning electron microscope equipped with a solid-state X-ray detector revealed that the second phase particles were sulfur-rich (Fig. 22). Furthermore, the second-phase particles appeared to have a lower thorium content than the matrix grains.

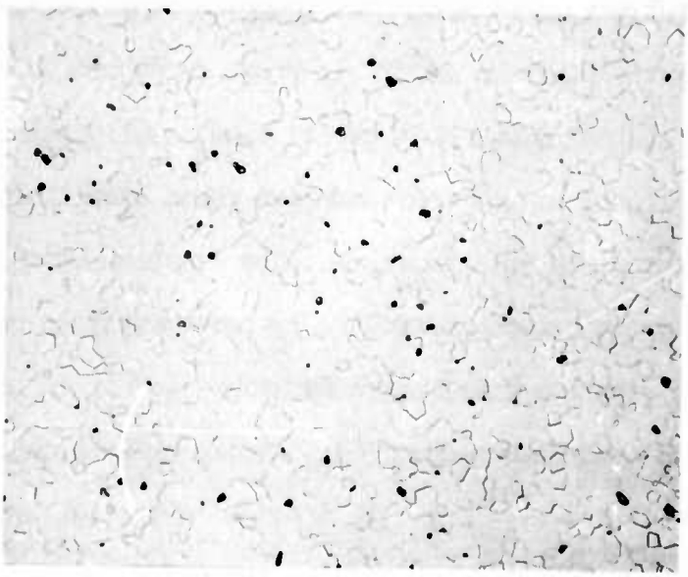

Figure 20 Microstructure of NDY ceramic illustrating pore-grain boundary configuration. Specimen prepared from unmilled powder and sintered 2 hours at 2000°C in dry H_2. Reflected light. 375X

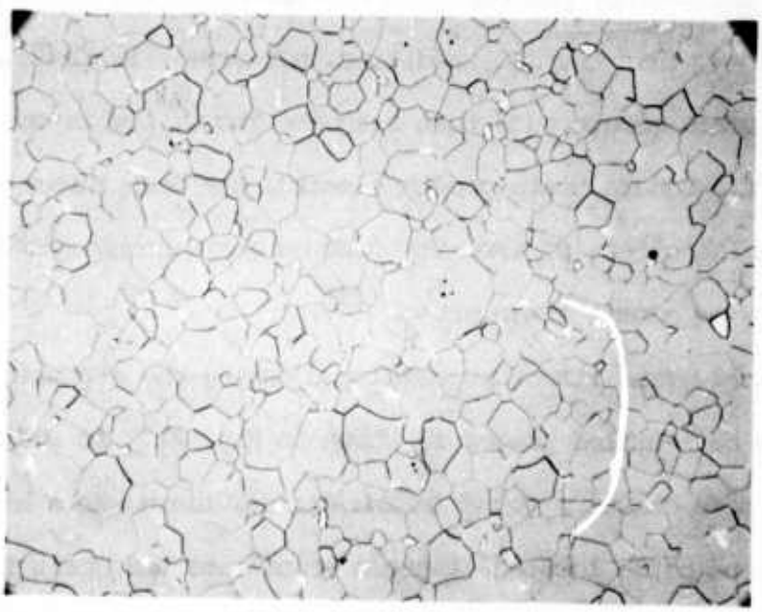

Figure 21 Grain structure in NDY ceramic sintered 2 hrs at 2000°C in wet H_2. Note highly reflecting, sulfur-rich second phase at grain boundaries and intersections, and occasional pore cluster inside grains. Specimen prepared from milled powder. Reflected light. 340X

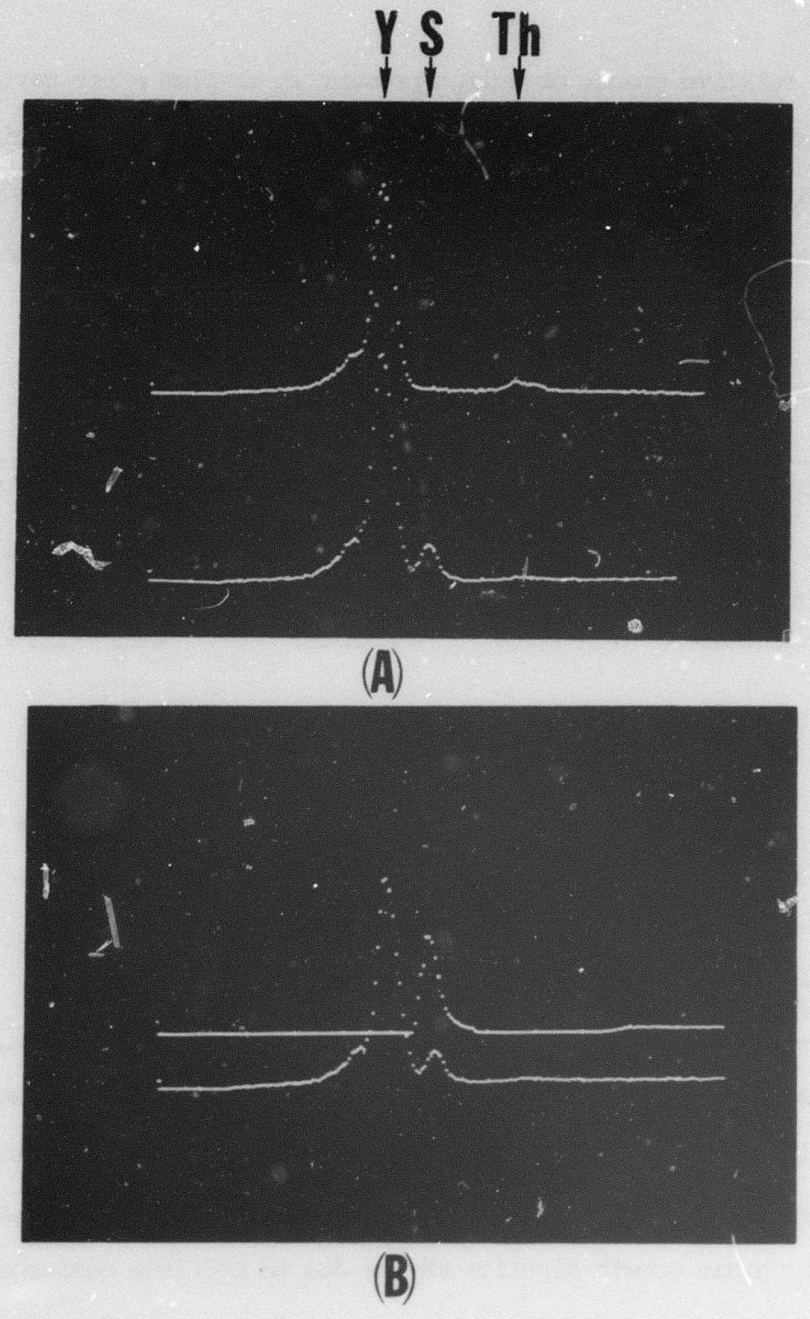

Figure 22 Solid-state X-ray spectra (on SEM) used to identify composition of second phase inclusions. (A) A NDY matrix grain (upper spectrum) and a second phase inclusion (lower spectrum). (B) Zinc sulfide sulfur standard (upper spectrum) and second phase inclusion (lower spectrum).

The relative amount of sulfur present in samples after various stages of powder processing and sintering treatment was determined by a standard combustion test and is given in Table II. The source of sulfur was from the abrasion of the vulcanized rubber-lining of the ball mill which contained about 2 wt % sulfur.

TABLE II

Sulfur Content in ThO_2-Doped Y_2O_3 After Various Stages of Powder Processing or Sintering Treatment

Powder Processing	Sintering Treatment	Sulfur Content (ppm)
Oxalate powder, calcined 4 hrs @ 800°C	--	40
Ball-milled calcined powder, 6 hrs	--	2200
Ball-milled calcined powder, 6 hrs	11 hrs @ 2115°C	370
Ball-milled calcined powder, 6 hrs	125 hrs @ 2170°C	40

The mechanism of grain growth in sulfur containing NDY ceramics at 2000°C is not exactly known but may be related to the inhibition of grain boundary movement by solid second-phase particles. The cubic relationship found for grain growth kinetics may be due to particle coalescence by a solution and reprecipitation phenomena similar to that described in the literature[14]. For the same time and atmosphere at 2000°C, sulfur-containing NDY ceramics have a larger average grain size because discontinuous grain growth occurs very early during the final stages of sintering and is evidenced by the presence of pore clusters entrapped inside grains (Fig. 21).

After the occurrence of discontinuous grain growth, there is a new generation of grains in which continuous grain growth occurs in the presence of second-phase particles. It is observed, however, that the sulfur-rich second phase slowly disappears upon prolonged heating at 2000°C and at higher temperatures. The sulfur is incorporated into second phase particles at T <2100°C and into an intergranular liquid phase at 2100°C < T < 2220°C. Sulfur is removed during the sintering process and causes the second phase to act as a transient phase during microstructural development. Although cubic grain-growth kinetics is observed in sulfur-containing NDY material over the time interval investigated at 2000°C, square-grain-growth kinetics are found for the same material at 2170°C for the time interval investigated. The reason for this observation is that for prolonged anneals at 2170°C most of the sulfur has diffused out of the sintered specimen. This is supported by X-ray diffraction, reflected light, and transmitted light microscopy of polished sections.

The final stage sintering kinetics of NDY ceramics containing 10 mole % ThO_2 were measured by the CCl_4 displacement method. For compacts sintered at 2000°C in wet and dry H_2, there was a linear fit of the data when relative density is plotted against logarithm of time. There was little difference in the sintering kinetics of specimens sintered in wet and dry H_2. The sintering kinetics apparently follow Coble's model[15] of final stage sintering in which closed pores located on 4-grain corners continuously shrink. Since microstructural observations show that grain and pore growth also occur in this stage of sintering, Coble's treatment cannot be applied to the data. Thus, the densification mechanism in NDY ceramics during final stage sintering has not been elucidated.

6. Kinetics of Pore Disappearance During the Late Final Stages of Sintering

It is generally accepted that pore removal during the late stages of sintering is diffusion controlled and that closed pores shrink by the transport of vacancies and soluble gas atoms from them to the grain boundaries. Furthermore, it is usually assumed that the direct flow of the rate-limiting species, which is usually presumed to be the entrapped gas, into a grain boundary along its intersection with a pore is negligible compared to the flow resulting from volume diffusion from the surface of the pore. In the very late stages of sintering in which the volume fraction of pores is of the order of 10^{-4} or less, pore-grain boundary interactions control sintering and pore-pore interactions are virtually minimized. The study of pore elimination in this regime of sintering offers the opportunity to make some deductions about the mechanism of pore shrinkage.

Several measurements of pore size frequency distribution were made on the same NDY sample during the course of prolonged heating at 2170°C in dry hydrogen. This material, prepared from ball-milled powder, is well-suited to the study of final stages of sintering because of its low pore density and high transparency. At the time the first measurements were made, after 33 hours at temperature, the average pore density was less than 1 per grain. The pore distribution was such that a few pores or a pore cluster were located inside an appreciable number of grains.

The data were obtained by measuring between 130 and 750 pores in about 0.75 to 3 mm^3 of solid and are shown in Fig. 23. The pore-size

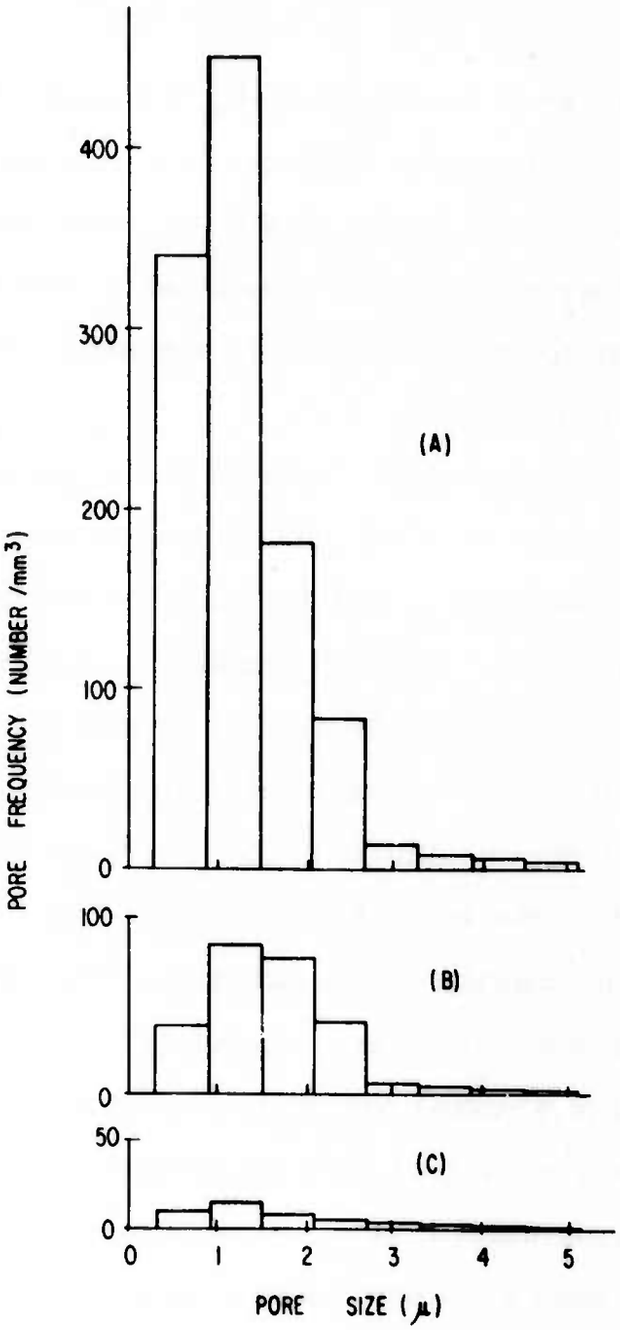

Figure 23 Pore density versus pore size in NDY ceramic sintered at 2180°C in dry H_2 (dew point ~ -70°C). (A) Specimen sintered 33 hrs and characterized by a grain size (D_g) of 110 μm and a volume fraction of pores (V_f) of 2.3×10^{-6}. (B) Specimen sintered 91 hrs having D_g = 190 μm and $V_f = 8.7 \times 10^{-7}$ (C) Specimen sintered 180 hrs having D_g = 260 μm and $V_f = 2.5 \times 10^{-7}$.

distribution is seen to remain essentially unchanged, whereas the pore density decreases with time of heating. Thus, it appears that pores are disappearing from the sample but that the pores observed at any time have not shrunk appreciably. This anomaly can be resolved by considering the grain growth that occured during the experiment. The grain growth data are shown in Fig. 19.

During the heating from 33 to 91 to 180 hours, the average grain size increased in the ration 1:1.73:2.36, respectively. On the average, then, the volume occupied by about 5.2 grains at 33 hours contained one grain after 91 hours. Similarly, about 13.3 grains at 33 hours were absorbed into one grain after 180 hours. If pores shrank rapidly when encountered by the migrating boundaries of the growing grains, it would be expected that the pore densities after 33, 91 and 180 hours of heating would be in the ratio of 1:0.19:0.07, respectively, assuming a uniform pore distribution inside each grain. The experimentally-measured ratios were 1:0.23:0.04, respectively. Thus, it appears that essentially all pore removal occured as a result of rapid disappearance of pores on grain boundaries. This conclusion is reinforced by observations of pore clusters during the experiment. Such clusters appeared to maintain a constant number of pores in a wide range of sizes throughout the experiment, indicating that gas flow between pores inside grains and from these pores to grain boundaries was negligible.

The qualitative picture of the mechanism of pore elimination caused by grain boundary migration is illustrated in Fig. 24. In Fig. 24 A, it is

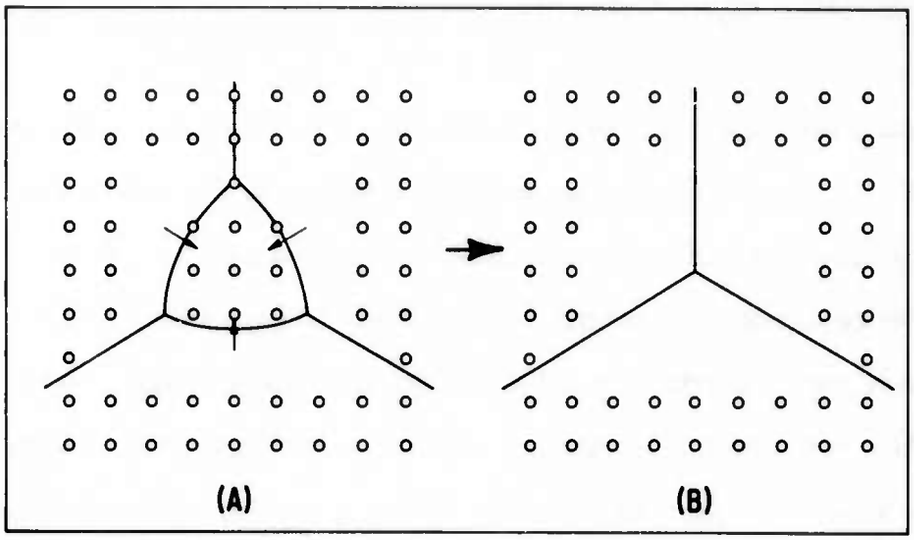

Figure 24 Qualitative mechanism of pore elimination by grain boundary migration. (A) Pores, initially located inside shrinking grain, interact with grain boundaries migrating towards their center of curvature. (B) Preferential pore elimination in that volume swept by migrating grain boundaries.

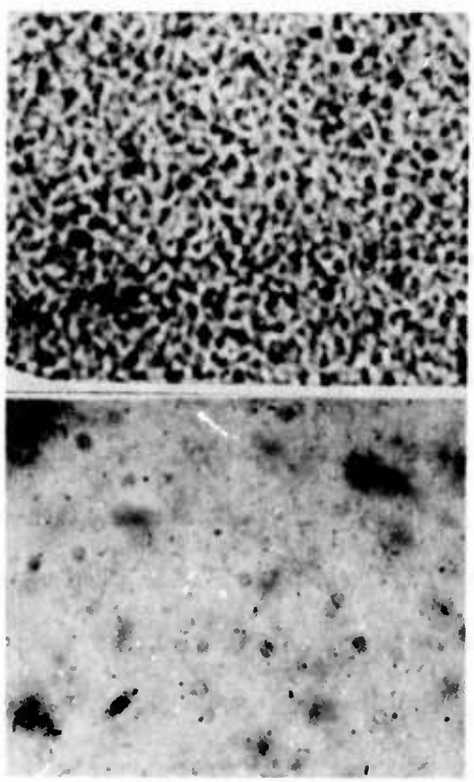

Figure 25 "Orange Peel" in sintered material prepared from (A) unmilled powder (upper) and (B) milled powder (lower), oxalate process. Polished specimens of equal thickness (~1/16 inch). Transmitted light.

assumed that there is a uniform distribution of equal-sized, spherical pores in all grains and that pores on grain boundaries are spherical. Some grains, having less than six sides in cross-section, shrink by the migration of their boundaries toward the center of curvature during grain growth. In this process, pores located inside a shrinking grain eventually meet a grain boundary and rapidly disappear. After the 3-sided grain disappears in Fig. 24 B, there is a pore-free region in the vacinity of the resulting triple point. Those pores which do not encounter a migrating grain boundary remain relatively unchanged in size and number.

The observations on pore disappearance at grain boundaries also imply that volume diffusion is not the primary mechanism by which such pores lost hydrogen gas to the boundary. The ratio of the final to initial heating times in this experiment is equal to about six, and the results given by theoretical calculations[17] indicate that considerable shrinkage of the pores inside grains should have occurred in this time if the pores on boundaries had disappeared by volume diffusion. Since this did not happen, and since all the observations indicate that the rate of shrinkage of pores on boundaries was much faster, perhaps by an order of magnitude or more, than the values calculated for equivalent pores inside grains, one is led to conclude that some other mechanism besides normal volume diffusion must have dominated the shrinkage of such pores. A possible mechanism that would lead to rapid shrinkage of closed pores on grain boundaries is that of direct passage of gas into a grain boundary along its interseciton with the pore. Shrinkage rate controlled by a grain-boundary diffusion mechanism has previously been proposed to be operating during the initial and intermediate stages of sintering.[18,19,20]

B. ORANGE PEEL

Good optical quality, sintered specimens prepared from unmilled calcined powder generally contain a considerable degree of "orange peel," which is an optical waviness or distortion in the sample as detected by the unaided eye. Orange peel can also be observed at low magnifications with the optical microscope by using a pinhole source of transmitted light (Fig. 25A). It is evidenced qualitatively by a black and white "grainy" texture as the specimen surface is viewed slightly out of focus.[8] The unaided eye cannot clearly detect an object at the opposite end of a polished rod 3" in length while viewing through it because of orange peel. It was discovered, however, that sintered rods made from ball-milled powder contained very little orange peel (see Fig. 25B), and the unaided eye could resolve an object at a distance of a few miles through a 3-inch-long rod.

The above observations indicated that orange peel may be related to chemical inhomogeneities (Th^{4+}/Y^{3+} ratio differences) formed in various regions of the oxalate percipitate during powder preparation. This reasoning is supported by the fact that orange peel is reduced by screening or ball-milling the oxalate and/or the calcined powder before powder compaction. Both processing steps have a tendency to reduce compositional variations on a large scale in the starting powder and to promote a faster approach to chemical equilibrium by interdiffusional processes during sintering at high temperatures. Further supporting evidence of chemical segregation present in the starting powder was revealed by X-ray diffraction analysis which showed that the calcined powder contains a trace of a ThO_2-rich phase.

If orange peel is caused by chemical segregation in the starting powder

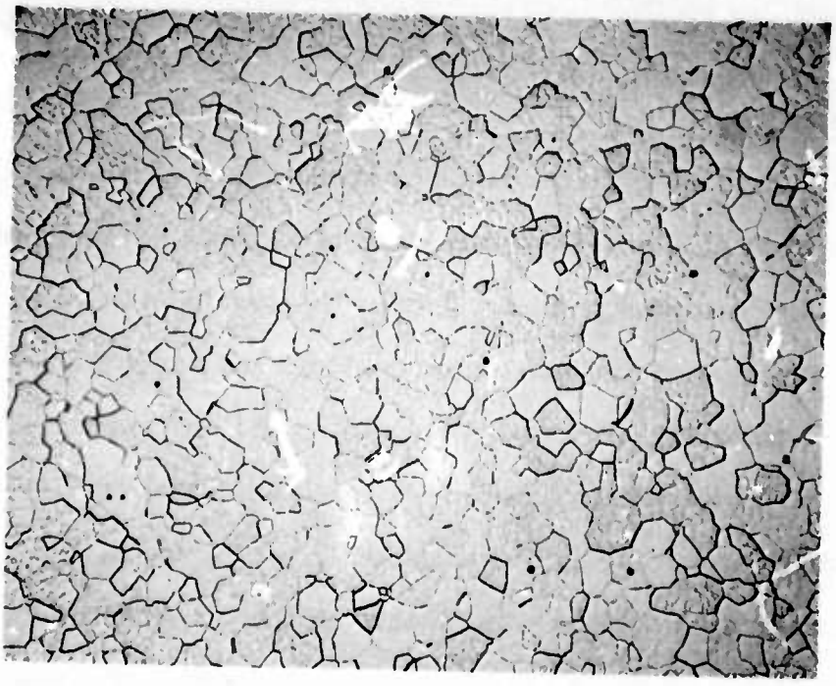

Figure 26 Substructure in sintered NDY ceramic prepared from oxalate powder made by pouring Y-Th-Nd salt solution into an oxalic acid solution. Sintering treatment 8 hrs at 2000°C. Chemically-etched for 1 min. in 1 part H_2O and 1 part HCl (boiling).

390X

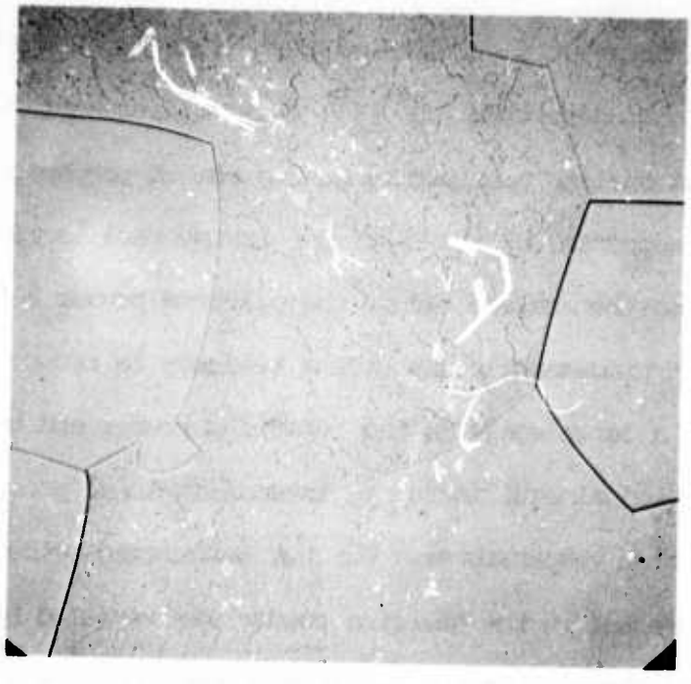

Figure 27 Substructure in sintered NDY ceramic prepared from milled calcined powder derived from the standard oxalate method. Sintered 38 hrs at 2170°C, fast-cooled to room temperature and chemically-etched for 1.5 min. in boiling 1 part H_2O + 1 part HCl.

390X

which does not completely homogenize in specimens sintered at temperatures 95% of the melting point for extended times, then an X-ray diffraction analysis of specimens containing different amounts of orange peel might reveal composition variations within the solid solution matrix of NDY ceramics. An experiment was carried out in which two NDY rods were fabricated from the same powder batch having the composition 89 mole % Y_2O_3, 10% ThO_2 and 1% Nd_2O_3. These rods, one prepared from unmilled calcined powder and the other prepared from milled calcined powder, were sintered under identical conditions (38 hrs at 2170°C in dry H_2) and cooled identically to room temperature. The sintered specimens were crushed and ground identically under alcohol with an agate mortar and pestle for 10 min. so that the powder particles passed through a 325-mesh nylon screen. X-ray diffractometer traces were obtained from both powder samples using identical preparation and operating conditions. Slow X-ray scans (1/4° 2θ/min.) were made of the Y_2O_3 solid solution peaks which occur in the 2θ region between 151° and 160°. For all six peaks (CuK_{α_1} and CuK_{α_2}) found in this region, the full width at half maximum intensity of each peak was approximately 20% larger for the powder sample of the sintered rod initially prepared from unmilled powder than for the corresponding diffraction peaks obtained from the powder sample of the sintered rod initially prepared from ball-milled powder. In addition, the 2θ positions of the corresponding diffraction peaks obtained from both powder specimens were virtually identical. These findings strongly indicate that this X-ray line broadening is caused by nonuniform strain associated with composition fluctuations in the cubic solid solution matrix which gives rise to refractive index variations causing the optical phenomenon called "orange peel."

Additional evidence of orange peel in sintered NDY ceramic containing 10 mole% ThO_2 was obtained by chemically etching a well-polished surface with boiling 1 part HCl + 1 part H_2O for 1 to 1.5 minutes. The amount of orange peel in NDY ceramic was intentionally exaggerated to reveal subtle differences in the etching behavior of different regions within the grains. (Orange peel was exaggerated by synthesizing a starting oxalate powder by a method in which the Y-Th-Nd salt solution was poured slowly into a vigorously stirred oxalic acid solution). A chemically etched, polished section of the sintered material made from unmilled powder is shown in Fig. 26. Note that a substructure is clearly revealed in most grains in this specimen (average grain size ~10μm). Close examination of the microstructure at magnifications up to X1000 showed that virtually all grains contain substructure. The revelation of substructure is more apparent in some grains than in others and may be related to the effect of chemical etching on grain orientation.

The substructure within the grains is characterized by irregularly shaped regions up to about 5μm in size which, in several instances, appear to interconnect from one grain to another without any regard for the grain boundary. Such grains, apparently, have nearly the same crystallographic orientation and chemically-etch at about the same rate so as to reveal this substructural appearance. On this basis, it seems that the origin of the substructure occurred very early in the development of the microstructure and is probably related to the presence of chemical segregation in the starting powder. In many cases, nearly spherical regions about 1 or 2μm in size are observed inside grains and could be the remnants of the original powder particles having variable composition. It is suggested that rapid grain growth took place during the early stages of

sintering and left behind the trails caused by chemical segregation. It is surprising that these small compositional or impurity differences do not disappear even after prolonged firing times at temperatures near 95% of the melting point. For example, Fig. 27 shows a chemically-etched microstructure of an Yttralox sample which was prepared from milled powder, sintered for 38 hours at 2170°C, and then cooled rapidly to room temperature. Specimens cooled slowly to room temperature give rise to the same type of microstructure. The substructure is again pronounced in some grains but there is not as much coarseness to the substructure as is evident in Fig. 26. It appears that the coarseness of the substructure is related directly to orange peel which is caused by chemical segregation of yttria and thoria in the starting calcined powder. The substructure is not composed of low angle grain boundaries, or subgrains, because electron transmission and diffraction results showed no evidence of dislocation networks outlining subgrain boundaries or of any detectable difference in crystallographic orientation with position inside a grain.

An investigation was undertaken to develop improved powder preparation procedures to reproducibly fabricate NDY ceramic with reduced orange peel. Several changes were made in the oxalate precipitation method in order to more thoroughly explore this method. The influence of drop size, temperature, molarity and nominal composition of the Y-Th-Nd nitrate salt solution on orange peel in the sintered product was investigated. The results of this investigation can be summarized as follows.

(1) An airosol technique using a high velocity air stream was developed to decrease the droplet size of the Y-Th-Nd salt solution from the millimeter size range (as is present in the standard drip method) to the micron size range before reacting with oxalic acid to form the oxalate precipitate. For a given composition

there was less orange peel in sintered material produced from unmilled powder by using the airosol method rather than the drip method.

(2) Hot (85°C) nitrate salt solution dripped into a cold (5°C) oxalic acid solution gave rise to sintered material (prepared from unmilled powder) which contained less orange peel than that produced by the standard drip method employed at room temperature.

(3) A Y-Th-Nd oxalate precipitate, synthesized by the drip method by changing the concentration of the nitrate salt solution from 1.1 g/cc to 0.11g/cc, did not give rise to sintered material with less orange peel.

(4) For a given variation of the oxalate precipitation method without using a ball-milling step, nitrate compositions richer in thorium generally gave rise to sintered specimens having more orange peel. The compositions investigated were (a) 89 mole% Y_2O_3 + 10% ThO_2 + 1% Nd_2O_3, (b) 94mole% Y_2O_3 + 5% ThO_2 + 1% Nd_2O_3 and (c) 96.5 mole% Y_2O_3 + 2.5% ThO_2 + 1% Nd_2O_3.

(5) The average size and morphology of the oxalate particles synthesized by the various methods of powder preparation were virtually the same as that shown in Fig. 5A.

Evaluation of these experimental findings for unmilled powder suggest that (1) a decreased size or an increased surface area of the nitrate

droplets favors a faster reaction rate with the oxalic acid and forms oxalate particles with more uniform composition and dispersion, (2) by dripping hot nitrate solution into a cold oxalic solution, the viscosity of the nitrate solution may be reduced so that there is an increase in the flux of yttrium and thorium ionic complexes reaching the nitrate droplet/oxalic acid solution interface, thereby reducing the chance of chemical segregation, and (3) chemical segregation apparently increases with increasing ThO_2 content.

Although chemical segregation of Yttrium and Thorium can be changed somewhat by certain variations of the oxalate precipitation approach, the most efficient way to markedly reduce these chemical inhomogeneities to date is by dry ball-milling either the oxalate powder before calcination or the calcined powder in the presence of 1 wt % stearic acid in a rubber-lined mill. The possibility of preparing NDY powder by freeze-drying or other wet-chemical approaches is currently under investigation.

VI. OPTICAL MEASUREMENTS

A. Spectral Transmittance

Sintered Yttralox and Nd-doped Yttralox ceramics can be produced with unusually high optical transparency by an oxalate approach provided that careful powder preparation and processing are employed to minimize impurities, large pores and pore clusters, and chemical segregation effects and provided that the stoichiometry is controlled by a proper sintering atmosphere. After sintering at 2170°C for 30 to 60 hrs. in wet H_2, Yttralox ceramic containing 10 mole% ThO_2 is a single phase, cubic solid solution with a grain size between 100 and 150μm. In Fig. 28 the spectral transmittance of Yttralox ceramic is shown along with several other commercially available materials having potential application as high-power infrared

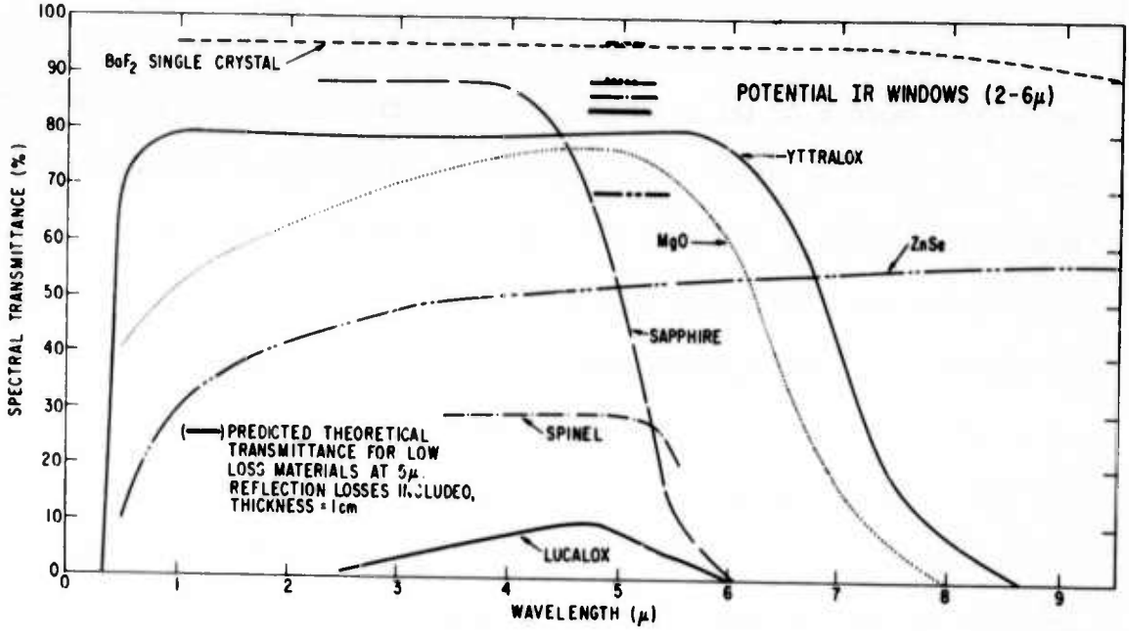

Figure 28 Spectral transmittance of Yttralox ceramic compared to some commercially available materials considered for IR windows.

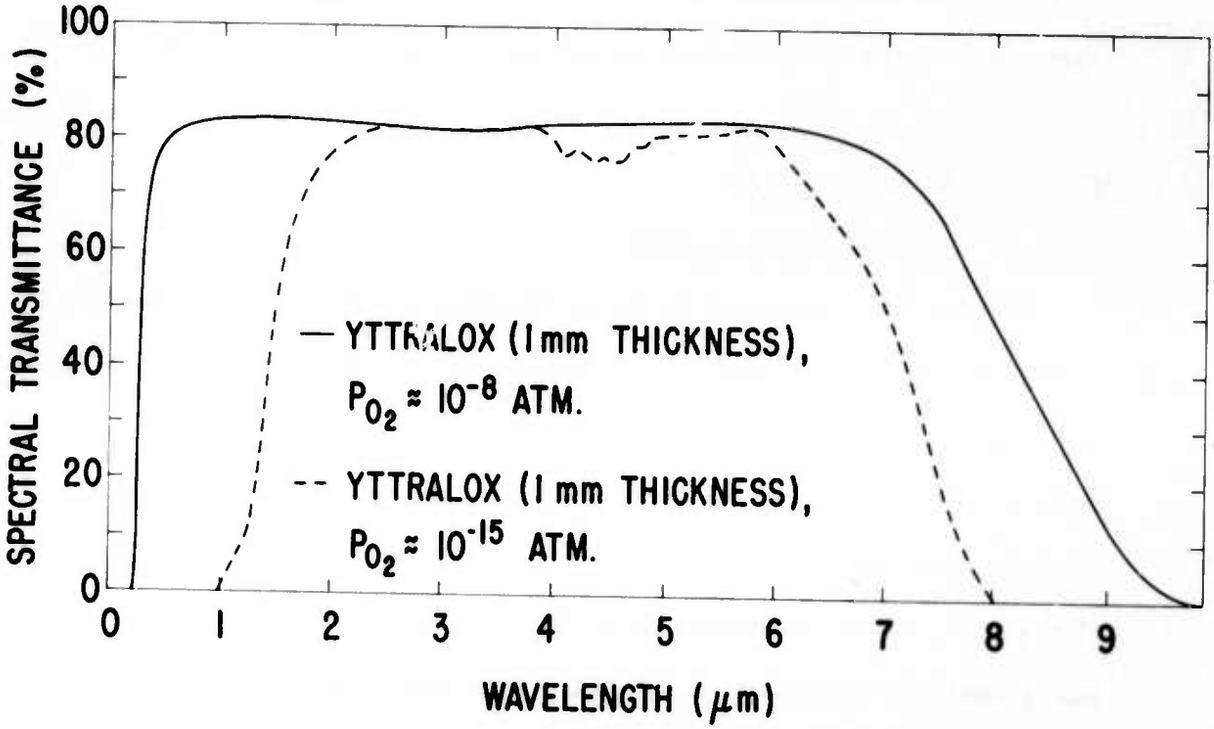

Figure 29 Influence of sintering atmosphere on the spectral transmittance of Yttralox ceramic.

windows for the 2 to 6μm region. The spectral curves are normalized for 1 cm thick plates. Note that Yttralox ceramic is transparent between 0.25 and 9μm with no absorption bands. The horizontal line segments at 5μm represent the theoretical transmittance predicted for the respective material having a negligible attenuation coefficient. Note that the difference between the predicted value for theoretical transmittance and that measured experimentally at 5μm (CO laser wavelength) is smaller for Yttralox ceramic than for the other transparent polycrystalline materials, indicating the superior optical quality of Yttralox ceramic. Likewise, Yttralox ceramic has higher light transmittance in the visible region than the other polycrystalline materials shown here. Single crystals of some of the halides and oxides, such as BaF_2 and Al_2O_3, can be made, of course, with excellent optical quality.

Controlled oxidation of Nd-free Yttralox ceramic at high temperature can generate a pronounced middle infrared pass filter or a visible-to-middle infrared pass filter. Spectral transmittance of Yttralox ceramic (90 mole% Y_2O_3 + 10% ThO_2) sintered in wet H_2($PO_2 \simeq 10^{-8}$ atm) and in dry H_2 ($PO_2 \simeq 10^{-15}$ atm) at 2170°C were measured with Cary Model 14 and Perkin-Elmer Model 521 spectrophotometers (See Fig. 29). For a 1 mm thick plate, the short and long wavelength cutoffs are 0.25 and 9.5μm for material fired in wet H_2 and 1 and 8μm for material fired in dry H_2 at 2170°C. The color of Yttralox fired in wet H_2 is water-white, whereas that of material fired in dry H_2 is black. Both clear and black materials are cubic single phases, as ascertained by X-ray diffraction analyses using the Debye Scherrer method, and have lattice parameters of 10.6496 ±0.0007Å and 10.6476 ± 0.0005Å, respectively. The black color and the slightly smaller unit-cell associated with this yttria base solid solution fired in low PO_2 atmospheres are related probably to the removal of a considerable

number of oxygen ions from the lattice, causing possible F-center formation in which oxygen vacancies trap electrons.

The high spectral transmittance in the 1μm region makes Yttralox ceramic a promising laser host for the Nd^{3+} ion. A comparison of the absorption spectra for NDY ceramic and two commercially available laser materials, Nd:YAG single crystal and Nd:glass, is shown for the wavelength region between 0.54 and 0.94μm in Fig. 30. The absorption spectra were obtained on YAG single crystal, glass and NDY ceramic containing 1.4×10^{20}, 2.8×10^{20} and 2.8×10^{20} Nd ions/cm^3, respectively, and having a plate thickness of 5, 6.3 and 6.3mm, respectively. NDY ceramic has broader absorption bands than Nd:YAG, but not as broad as Nd:glass. Broad, intense absorption bands of the Nd^{3+} ions at frequencies above the lasing frequency are required for efficient utilization of the flashlamp energy so that a large population inversion of electrons may be achieved between the $^4F_{3/2}$ and $^4I_{11/2}$ energy levels responsible for the lasing transition. The absence of an absorption band in the lasing wavelength region of 1.06 to 1.08μm (not shown in Fig. 30) indicates that the electron population in the $^4I_{11/2}$ level is very small for the three materials investigated.

B. Optical Quality

The optical quality of neodymium-doped Yttralox (NDY) rods was compared to that of Nd-doped YAG single crystal and Nd-doped glass rods using a Twyman-Green interferometer. The YAG and glass rods were 7.62 cm in length and 0.625 cm in diameter, whereas the NDY rods were 7.62 cm in length and approximately 0.5 cm in diameter. These rods had ends flat to λ/10, using Na light with λ= 5898Å, and ends parallel to ± 2 arc seconds while maintaining perpendicularity to the rod axis.

The rods were examined with a double-pass Twyman-Green type interferometer operated with an He-Ne laser source (λ = 6328Å). Interfero-

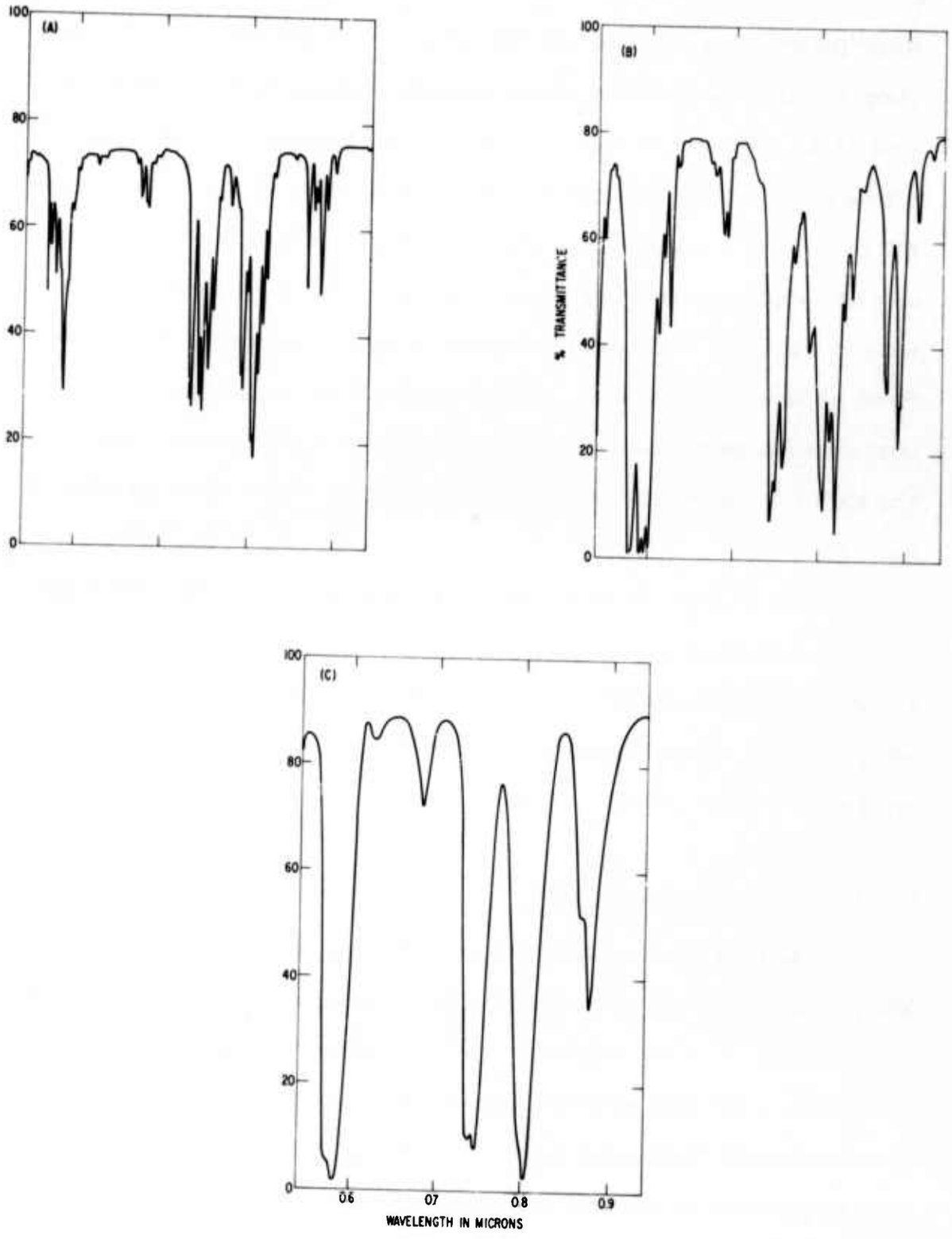

Figure 30 Absorption spectra for (A) Nd:YAG, (B) NDY ceramic and (C) ND:glass in the visible and near-infrared regions at room temperature. Nd-concentrations and plate thicknesses are given in the text.

meter patterns for Nd-doped YAG rod (SIZ-Grade, Union Carbide), Nd-doped glass rod (ED-2 Laser glass, Owens Illinois) and Nd-doped Yttralox rod (YTC 13-4) are shown in Fig. 31. The optical quality, determined by fringe count, of the NDY rod was comparable to that of the presently available YAG rod, about 1 fringe across the diameter of the rod, but not as good as glass which has approximately 1/5 fringe across the diameter. Glass rods of this size will normally exhibit no distortion except that introduced by imperfect finishing of the rod ends. The majority of Yttralox rods examined exhibited about 1 to 3 fringes of a random nature across the rod diameter whereas the interference pattern for YAG was somewhat non-uniform.

NDY rods observed in polarized light using crossed nicols give rise to weak, cross-type interference figures which indicate that there is residual stress in the rods. Under similar conditions, a cubic Nd:YAG single crystal rod also exhibits an interference pattern. A glass laser rod, on the other hand, shows no evidence of birefringence.

C. Nd Fluorescence Emission

Fluorescence spectral measurements were made on an NDY rod and a Nd:YAG rod possessing the Nd concentrations mentioned above. The NDY rod contained 10 mole% ThO_2 in solid solution. The fluorescence was excited with 200 watts from a 500 watt tungsten incandescent lamp to obtain the best compromise between fluorescent output and ability to maintain the samples near room temperature by means of forced air cooling. In an attempt to minimize the effect of different rod diameters, a limiting aperature 0.36 cm in diameter was placed over the rod end. Fluorescent radiation passing through the aperture was collected and imaged on the entrance slit (0.4 mm slit

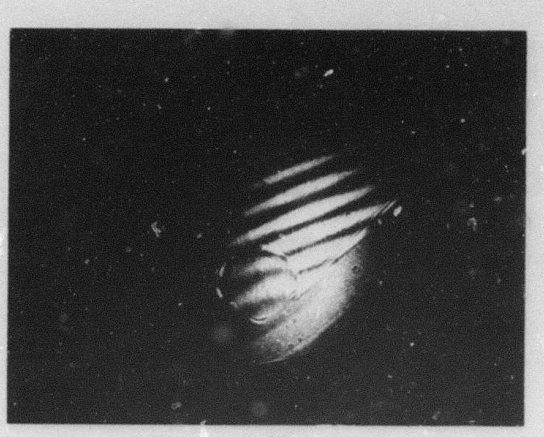

(A)

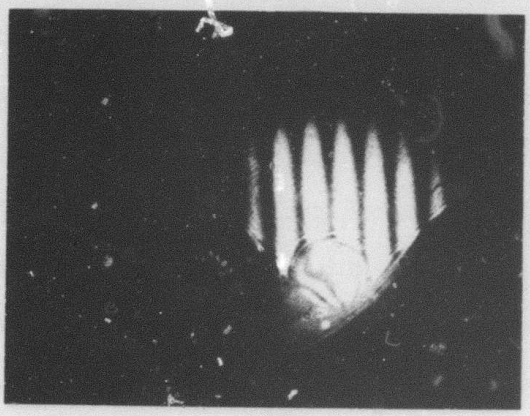

(B)

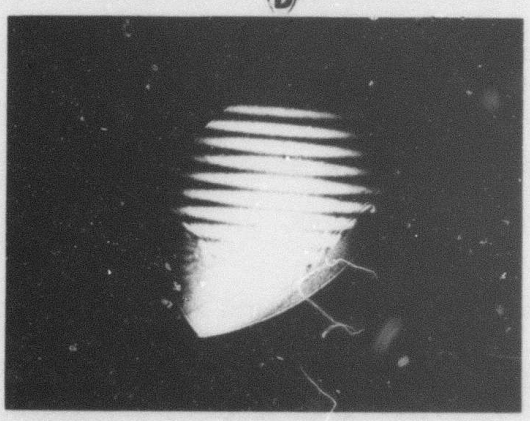

(C)

Figure 31 Twymann-Green interferometer patterns for (A) laser glass, (B) Nd:YAG and (C) NDY ceramic. Patterns show fringes in rods and visible background fringes.

width) of a Perkin-Elmer Model 13 double-pass grating monochromator. A PbS detector and Perkin-Elmer Model 107 amplifier were employed. The slit width was found to correspond to a spectral linewidth at half-peak intensity of approximately 0.2 nm. The spectra were corrected for spectral response of the system.

Fluorescent transitions for Nd:YAG and NDY ceramic are shown between 1.05 and 1.13 μm in Fig. 32. The Nd:YAG and NDY ceramic lasers operate primarily at a wavelength of 1.064 and 1.074 μm, respectively, at room temperature. The fluorescent emission spectrum for NDY ceramic is broader than that of Nd:YAG. At the respective lasing wavelength, the fluorescent linewidth (full line-width at half peak intensity) of NDY ceramic is about 3 nm or about six times larger than that of Nd:YAG. Since Nd:glass has a fluorescent emission linewidth of ≈26 nm and since the gain coefficient of laser radiation is inversely proportional to the linewidth, NDY ceramic is an intermediate gain material between that of Nd:YAG and Nd:glass.

NDY laser rods can be synthesized as controlled variable gain lasers because the fluorescent linewidth of the Nd^{3+} ions at the lasing wavelength increases linearly with increasing ThO_2 content (see Fig. 33). This relationship can be described by the equation

$$\Delta\lambda = \Delta\lambda_0 + 2.14X, \qquad (1)$$

where $\Delta\lambda_0$ is the linewidth at X = 0 and X is the ThO_2 content (in mole %) dissolved in the Y_2O_3 lattice containing a fixed amount of Nd_2O_3, 1 mole % or 2.8×10^{20} Nd^{3+} ions/cm^3. Note that the fluorescent linewidth can be increased by a factor of about 3 from 11.6 Å (X = 0) to 33 Å (X = 10) when going from ThO_2-free Y_2O_3 to Y_2O_3 containing 10 mole % ThO_2 in solid solution.

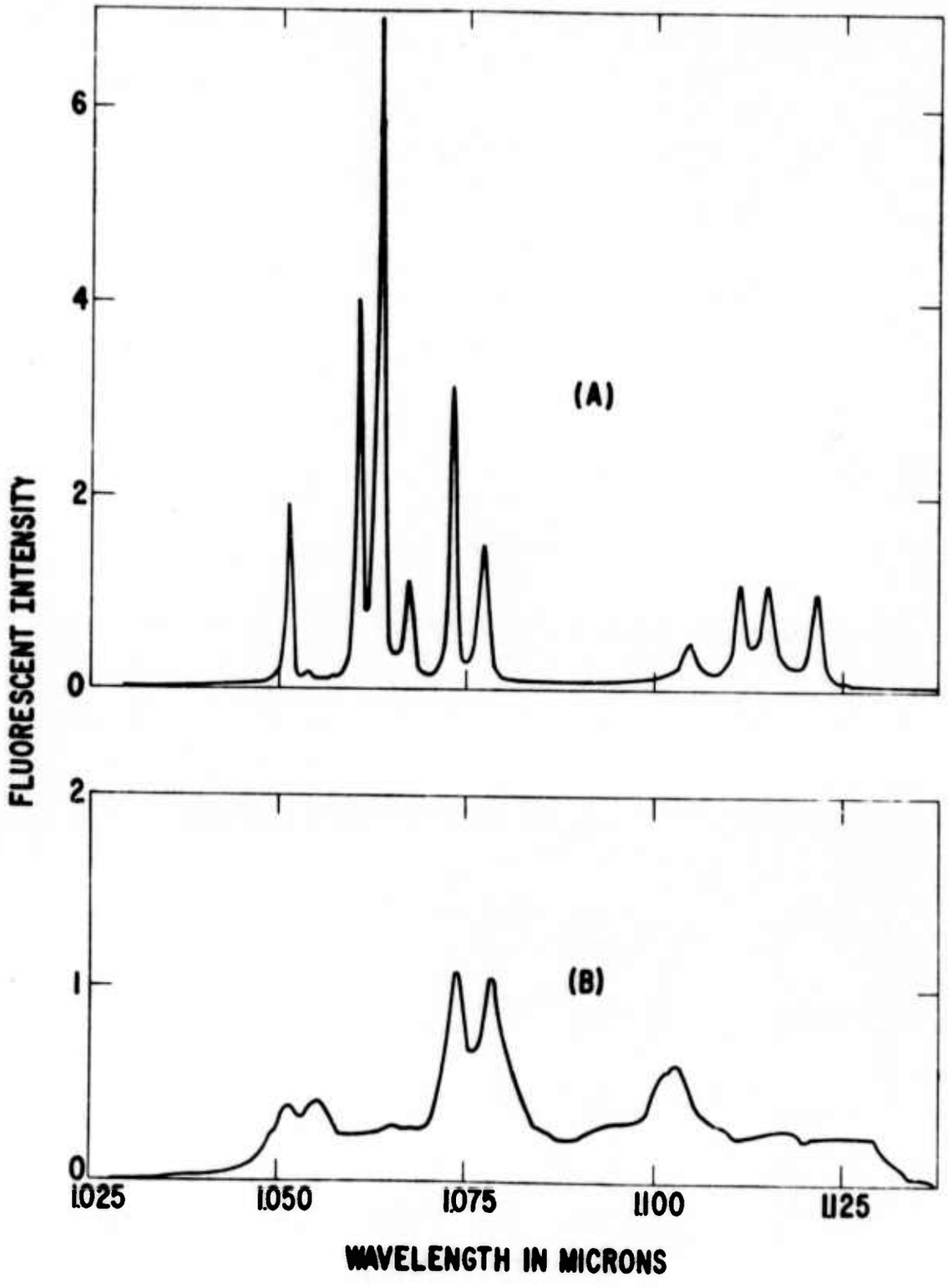

Figure 32 Fluorescence spectra of (A) Nd:YAG and (B) NDY ceramic in the 1 micron region at room temperature.

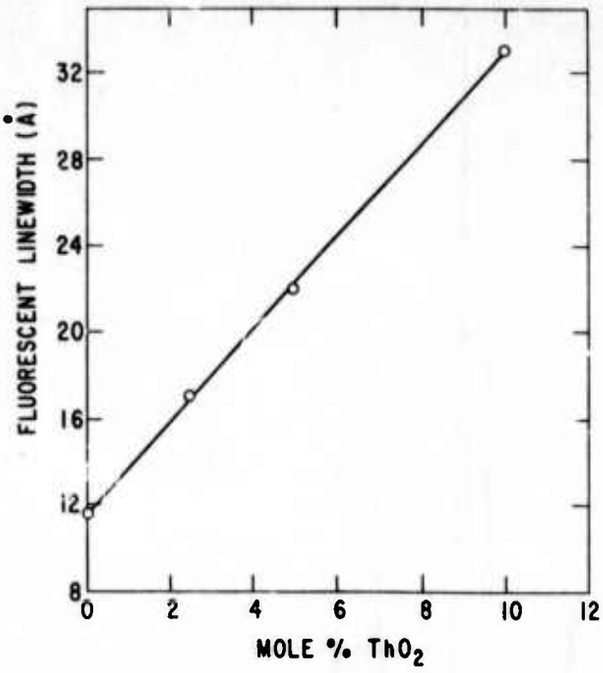

Figure 33 Fluorescent linewidth at $\lambda = 1.074$ as a function of ThO_2 content in NDY ceramic.

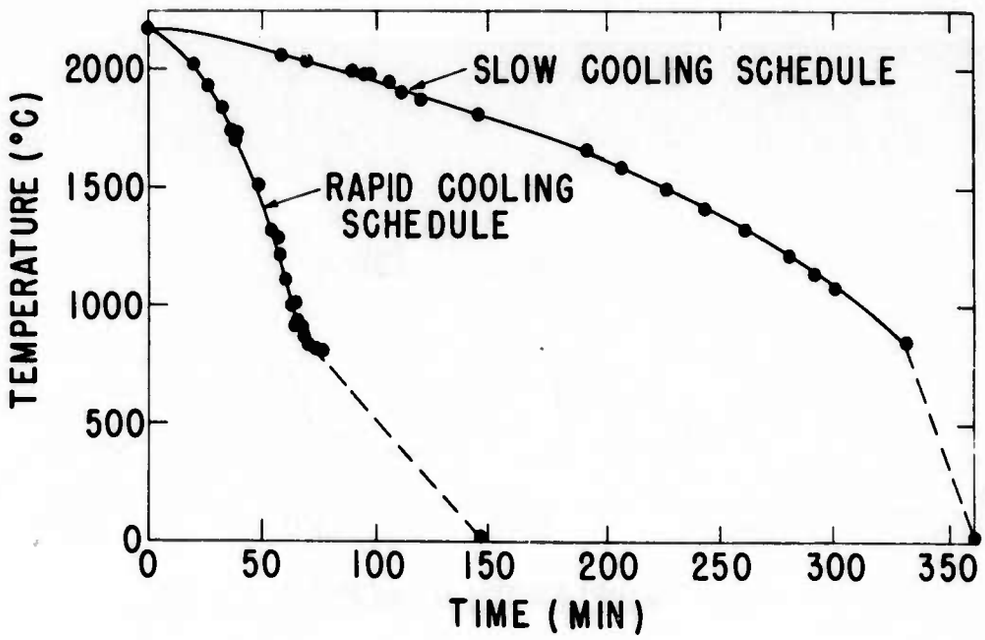

Figure 34 Slow and rapid cooling curves for NDY ceramic. Dashed part of the curve is an approximation.

No other solid state laser material is known to have been synthesized with such a large variable gain (inversely related to linewidth) caused only by changing the composition of the laser host. Furthermore, it is found that the position of this fluorescent band is independent of ThO_2 content.

The fluorescent linewidth at 1.074 μm is probably due primarily to inhomogeneous broadening of the Nd line which is caused by variations in the local crystal fields about the Nd^{3+} ions. This is associated with slight differences in the coordination sites of the Nd ions in the C-type rare earth structure of Y_2O_3. Besides the two types of octahedral coordination sites available for cations in this structure, [21] the substitution of Th^{4+} for Y^{3+} ions results in the introduction of oxygen interstitials which further modify the coordination environment about the Nd^{3+} ions. Therefore, the introduction of Th^{4+} ions, which occupy normal lattice sites, and interstitial O^{2-} ions (1/2 the number of Th^{4+} ions) which maintains electroneutrality of the crystal creates a random distribution of local crystal fields about the Nd^{3+} ions.

D. Optical Absorption at 1.064 μm

It is important to determine the optical absorption coefficient at the lasing wavelength so that an assessment can be made of the bulk losses in a laser material. In the case of Nd:glass lasers, it is generally accepted that the limiting optical losses are absoroption losses which can be as small as 0.1% cm^{-1} [22] but usually are higher and close to 0.25% cm^{-1} [6]. The absorption coefficient of Nd:YAG single crystal is not well established at 1.064 μm but the optical attenuation coefficient is generally taken to be 0.25% cm^{-1}. It was desirable to determine the absorption coefficient of NDY ceramic near the lasing wavelength of 1.074 μm so that a better interpretation could be made of the active attenuation coefficient determined from lasing experiments and so that a comparison could be made with that known for other laser materials.

The absorption coefficient of a NDY rod with ends flat and parallel were measured by a precision calorimetric technique recently developed.[23] The technique involves the careful alignment and thermal isolation of a NDY rod so that the optical power of a CW Nd:YAG laser (0.25 watts) passing through the rod will cause a detectable temperature rise (ΔT) in the sample. At steady state the rate of heat generation in the sample caused by optical absorption is balanced by the rate of heat leakage by free-air convection. By abruptly turning off the laser beam and measuring ΔT as a function of time (t) a cooling time constant (τ) can be calculated from the slope of a plot of $ln\ \Delta T$ vs. t. The optical absorption coefficient (α) is calculated from the equation

$$\alpha = C\ (\pi r^2)\ \Delta T_o / tP, \qquad (2)$$

where C is the sample heat capacity per unit volume, r is the radius of the

rod, ΔT_0 is the equilibrium temperature rise and P is the average optical power passing through the rod. The following values of the parameters were used for the calculation of α for a NDY rod which was rapidly cooled from the sintering temperature and contained 10 mole % ThO_2:

$$C = 0.24 \text{ cal/cm}^3\text{°C}$$

$$r = 0.267 \text{ cm}$$

$$\Delta T_0 = 1.05\text{°C}$$

$$t = 274 \text{ sec.}$$

$$P = 0.225 \text{ watts}$$

where C was measured by differential scanning calorimetry at 330°K. The absorption coefficient was calculated to be 3.8×10^{-3} cm^{-1} or $0.38\%cm^{-1}$ at λ = 1.064 μm. Since the lasing wavelength of NDY laser rods is 1.074 μm, it reasonable to assume that the absorption coefficient at 1.074 μm is virtually that measured at 1.064 μm. The absorption coefficient measured by this precision calorimetric technique generally represents an upper limit because it is difficult to eliminate surface contaminants on the rod. In comparison to Nd:laser glass, the absorption coefficient of NDY laser rods is about 50% higher at the lasing wavelength. It is not presently known what major impurities are responsible for most of the absorption but rare earth impurities originating from the starting yttrium nitrate powder are highly suspect.

E. Lasing Measurements in the Pulsed Mode Operation

1. Introduction

The attenuation of a beam of monochromatic radiation propagating through a laser rod can be determined by active laser measurements. Laser testing is a powerful means of investigating the influence of microstructural and submicroscopic defects on the optical perfection of NDY ceramic. Laser threshold energy is useful as a figure of merit to describe the optical perfection of the laser host and represents the condition at which the amplification of radiation in the laser rod is sufficient to compensate for the total optical losses in the system.

2. Experimental Procedures

Laser measurements were carried out in a pump cavity which consisted of a 2.54 cm diameter, silvered cylindrical reflector 5.62 cm in length. The flash lamp and laser rod were located symmetrically with respect to the cylinder center and spaced 0.95 cm apart. The flashlamp was a 4 mm bore xenon lamp with a 7.62 cm arc length of which only 5.62 cm was utilized in laser pumping. The lamp was energized by a 50 μf capacitor bank which produced a pump-pulse duration of 150 μsec. A Schott yellow glass filter was located between the flashlamp and laser rod to absorb radiation at wavelengths shorter than 500 nm. Filtering was required to prevent solarization of the NDY rods.

The laser resonant cavity consisted of two external dielectric mirrors having relectivities R_1 and R_2 and spaced 20 cm apart. The output mirror relectivity (R_2) varied from 50% to 95% whereas $R_1 \approx 100\%$ at a wavelength of 1.06 to 1.08 μm. Laser threshold energy was detected by the "spiking"

characteristics commonly observed in pulsed, solid-state lasers and defined as the minimum pump energy required to produce spiking or laser action at a given R_2- value. Lasing efficiency was determined from a linear plot of energy output as a function of pump energy input for R_2 = 80%. All NDY rods used for laser testing were 7.62 cm in length, whereas the laser glass (OI-ED-2) rod was 15.24 cm in length.

3. Laser Thresholds and Active Attenuation Coefficients for NDY Rods Containing 10 Mole % ThO_2

Table II shows that specimens 11-3 and 13-7 have relatively high porosities and high laser threshold values. Pores act as light-scattering centers and increase the material losses so that the flashlamp intensity must be increased to create a larger population inversion required to meet the threshold condition. Although the porosity in 13-4 rod is 2.5 times higher than that in 12-1 rod, the threshold value is observed to be lower. This anomaly may be explained by the fact that 13-4 rod contained a nonuniform distribution of pores of which approximately 10% of them were located within a 2 mm diameter, central core of the rod. Since only the central core of the rod generates laser radiation at the threshold condition,[24] 13-4 rod would be expected to give a smaller threshold value, even though the residual porosity is higher than that of 12-1 rod. Specimens 13-7 has an unusually large threshold value of greater than 100 joules because, in addition to porosity, there is a considerable amount of orange peel which markedly increases the optical loss of NDY ceramics. Orange peel in this sample could be detected by light scattering, transmitted light microscopy, and the unaided eye. Finally, although the threshold value of NDY ceramic

is predicted to be lower than that of laser glass:Nd because of its higher gain coefficient, these NDY rods have a higher threshold values caused by high optical losses, i.e. high γ values.

TABLE III.

Heat Treatment, Porosity, and Lasing Results for NDY Rods (Containing 10 mole % ThO_2) Relative to Laser Glass

Sample	Sintering Time at 2170°C (hr)	Porosity	Laser Threshold at 95% R_2 (J)	Active Attenuation Coefficient (%/cm)
11-3	58	3.2×10^{-6}	30	6.9
12-1	125	3.3×10^{-7}	21	5.4
13-4	80	8.2×10^{-7}	16	4.9
13-7	92	3.5×10^{-5}	>100	---
OI, ED2 glass	--	--	9	0.76

The"active" attenuation coefficient or material loss coefficient is obtained from laser threshold energies for different output mirror reflectivities. Laser threshold is given by the condition

$$\frac{1}{R_1 R_2} = \exp\left[(\sigma n - \gamma) 2l\right] \qquad (3)$$

where R_1 and R_2 are the mirror reflectivities, σ is the stimulated cross section, n is the inversion density of electrons caused by flashlamp radiation, γ is the active attenuation coefficient of the material, and $2l$ is the total optical path length. If $1/R_1R_2$ is plotted as a function of threshold energy

on a semi-logarithmic scale and extrapolated to zero flashlamp radiation or threshold energy, then for n = 0, the intercept along the ordinate gives

$$ln(1/R_1R_2) = -2\gamma l \ . \qquad (4)$$

Values of γ listed in Table III were determined from Eq. (2) by using the intercept method. NDY laser rods had active attenuation coefficients between about 5% and 7% cm^{-1} and these values were, on the average, about a factor of 8 higher than that of the glass:Nd rod. These high values of optical attenuation in NDY rods clearly indicate that the primary loss mechanism is due to scattering since the absorption coefficient is only 0.38 % cm^{-1} at λ = 1.064 μm. It should be emphasized that these NDY rods contain 10 mole % ThO_2 and were cooled from 2170°C to room temperature in approximately 6 hours.

A comparison of the absorption and total attenuation coefficients at 1.074 μm shows that one or more scattering mechanisms is responsible for most of the attenuation of laser radiation in NDY rods. A simple light scattering experiment which confirmed this finding was that when a He-Ne laser beam is passed through a rod, the rod appears bright in a dark background. If it is assumed that pores are the major scattering centers, then the attenuation coefficient can be calculated from light scattering theory assuming spherical, nonabsorbing pores which act as single scattering centers. Scattering losses per unit length ($-dI/Idl$) can be described by

$$-\frac{dI}{Idl} = \gamma = \sum_i n_i C_i \qquad (5)$$

where I = beam intensity (joules/sec cm^2) at a given value of l and wavelength,

on a semi-logarithmic scale and extrapolated to zero flashlamp radiation or threshold energy, then for n = 0, the intercept along the ordinate gives

$$ln(1/R_1R_2) = -2\gamma l \ . \qquad (4)$$

Values of γ listed in Table III were determined from Eq. (2) by using the intercept method. NDY laser rods had active attenuation coefficients between about 5% and 7% cm^{-1} and these values were, on the average, about a factor of 8 higher than that of the glass:Nd rod. These high values of optical attenuation in NDY rods clearly indicate that the primary loss mechanism is due to scattering since the absorption coefficient is only 0.38 % cm^{-1} at λ = 1.064 μm. It should be emphasized that these NDY rods contain 10 mole % ThO_2 and were cooled from 2170°C to room temperature in approximately 6 hours.

A comparison of the absorption and total attenuation coefficients at 1.074 μm shows that one or more scattering mechanisms is responsible for most of the attenuation of laser radiation in NDY rods. A simple light scattering experiment which confirmed this finding was that when a He-Ne laser beam is passed through a rod, the rod appears bright in a dark background. If it is assumed that pores are the major scattering centers, then the attenuation coefficient can be calculated from light scattering theory assuming spherical, nonabsorbing pores which act as single scattering centers. Scattering losses per unit length ($-dI/Id\ell$) can be described by

$$-\frac{dI}{Id\ell} = \gamma = \sum_i n_i C_i \qquad (5)$$

where I = beam intensity (joules/sec cm^2) at a given value of ℓ and wavelength,

n_i = number density of pores in a given size range (i), and C_i = the total scattering cross section over that size range. By using theoretical equations [25] of C_i for pores both small and large compared to the wavelength of light in an NDY laser rod, hypothetical plots of log C_i versus log d_i, where d_i is the average pore size over the size range (i), show that pores greater than about 0.3 μm follow the scattering behavior expected for large particles. This means that $d_i > 0.3$ μm, C_i is simply equal to twice the geometric cross section.[25] An error of about 10% is introduced if 2 is taken as the scattering efficiency factor. Under the above assumptions, and using Eq. (3), a theoretical γ-value of about 0.22% cm^{-1} was calculated for the pore size distribution microscopically observed in 12-1 rod (Fig. 9). The calculated value of γ is approximately a factor of 25 lower than the experimentally determined value of 5.4% cm^{-1}.

It was first thought that a considerable number of pores or solid second phase inclusions were present in sizes smaller than the detection limits of the optical microscope. The number of scattering centers, such as pores, less than 0.5 μm in size were determined in a given solid volume with the help of ultramicroscopy. Here, the sintered rod was illuminated by an intense beam of He-Ne laser light (1 mW output, λ = 632.8 nm) at 90° to the microscope optical axis. By focusing the microscope through the polished flat, second phase particles inside the specimen appeared as bright spots of scattered light against a dark field. The total number density of distinct microscopic and submicroscopic scattering centers was determined by counting bright spots while scanning through a known solid volume at a magnification of 460X. [Second-phase particles as small as 0.005 μm can be observed but not exactly measured with ultramicroscopy under good conditions.[26]] Finally, the number density

of submicroscopic scattering centers in a given rod was calculated by subtracting the number density of microscopic pores measured by transmitted-light microscopy from the total number density of scattering centers measured by ultramicroscopy.

The ultramicroscopy experiment showed that only about 20% of the total number of scattering centers observed were smaller than 0.5 μm in size, and such a small number of submicroscopic pores or solid second phase particles cannot account for the attenuation coefficient measured experimentally. In addition to the presence of distinct submicroscopic scattering centers observed as points of light under the ultramicroscope, a background haze was visible in the beam path traversing the specimen and suggested that the scattered light is weak and may be caused by submicroscopic scattering centers having a refractive index which is not very different from that of the matrix. If the visible haze is indeed real, then the origin of submicroscopic scattering centers in NDY ceramics may be caused by: (1) orange peel on a fine scale for which the interdiffusion flux for the constituent ions does not equal zero under the experimental conditions employed at the sintering temperature: (2) a gradient in oxygen from the specimen surface to center related to changes in the chemical potential of oxygen in the H_2/H_2O sintering atmosphere as a function of temperature during the cooling cycle; and (3) formation of submicroscopic ordered zones in the solid solution matrix during the cooling cycle. The scattering of light by grain boundaries in optically isotropic NDY ceramics is predicted to be negligible compared to other scattering effects, since a grain boundary free of gross segregation and solid second phase has a very small scattering cross section because its width is small compared to the lasing wavelength and its refractive index is close to that of the grain interior. In addition,

these NDY ceramics have large grain sizes ($\bar{>}$ 130 μm) so there is small grain boundary volume available for scattering.

Possiblities (1) and (3) mentioned above are most likely responsible for the formation of submicroscopic scattering centers in NDY ceramics because possiblity (2) cannot account for the brightness exhibited by a rod when placed in an He-Ne laser beam. If possibility (1) is the major cause of submicroscopic scattering centers, then the current method of powder preparation and processing does not achieve the distribution of Y^{3+}, Th^{4+}, and Nd^{3+} ions necessary to yield composition uniformity throughout the bulk of the material during the sintering process at temperatures 96% of the melting point. Segregation of Nd^{3+} ions is not believed to be responsible for orange peel because this optical phenomenon is also observed in Nd-free material produced from unmilled oxalate powder. In addition, the concentration of Nd^{3+} ions in these NDY ceramics containing 10 mole % ThO_2 in solid solution is only 1/5 that of Th^{4+} ions.

Possibility (3) is also highly reasonable. The Y_2O_3-ThO_2 phase diagram[1] shows that solubility of ThO_2 in Y_2O_3 decreases from approximately 13 mole % at 2200°C to 6 mole % at 1400°C. Since there is 10 mole % ThO_2 in the NDY laser rods discussed in this section, this solid solution crosses the solvus curve upon cooling from the sintering temperature of 2170°C. Although discrete precipitate particles are probably not formed during the cooling cycle, as ascertained by X-ray diffraction, transmitted-light and electron microscopy, and ultramicroscopy, coherent ordered regions may form in the solid solution matrix. These coherent regions, known as Guinier-Preston zones, Wadsley shear structures, or, more generally, extended defects, represent changes in structure

and composition which can produce fluctuations in local refractive index that scatter light. Such extended defects are coherent with the parent matrix and, as a result, are extremely difficult to detect by conventional methods.

An experiment was carried out to determine if the cooling cycle influenced the optical quality and lasing performance of NDY ceramic containing 10 mole % ThO_2. In particular, a rapid cooling technique was investigated in order to determine if it was possible to retard nucleation and growth of extended defects which may form variations in composition. The cooling curves generated under automatic programing conditions in a Brew[27] furnace are given in Fig. 34. The curve labeled "slow cooling schedule" represents the typical cooling schedule for all NDY laser rods cooled from 2170°C to room temperature in about 6 hours. Data points represent temperatures measured by optical pyrometry at various times; temperatures below 800°C could not be accurately measured with the optical pyrometer. After measuring the laser threshold, active loss coefficient and laser output efficiency on two rods, 12-1 and 13-4, these finished rods were individually reheated to the sintering temperature of 2170°C, equilibrated for only two hours so that very little sintering, if any, occurred, and then cooled according to the rapid cooling schedule to 800°C. It is believed that structural transformations below 800°C are minimal. Specimen preparation for lasing measurements was identical for both rods which shall now be designated 12-1A and 13-4A. Results of this study are shown in Table IV. The fast cooling schedule produces a significant reduction in the lasing threshold and active attenuation coefficient.

TABLE IV

LASER THRESHOLDS AND ATTENUATION COEFFICIENTS FOR NDY AND LASER GLASS RODS

Sample	Threshold at 95% R_2	Active Loss Coefficient
12-1	21	5.4% cm^{-1}
12-1A	17	4.5% cm^{-1}
13-4	16	4.9% cm^{-1}
13-4A	8	2.6% cm^{-1}
OI, ED2 Glass	9	0.76% cm^{-1}

For the case of 13-4B rod, the fast cooling treatment reduced the lasing threshold by 51% and the optical losses by 53%. Note that by fast cooling, 13-4A rod exhibits a lower threshold value than that of laser glass. Although a fast cooling schedule is desirable, there is a limit to how fast a rod can be cooled without fracture caused by thermal stresses. It is believed that the rapid cooling treatment permits retainment of the high-temperature, disordered solid solution and retards nucleation and growth of extended defects at lower temperatures. As a result, the rapid cooling schedule was adopted as a standard procedure in the synthesis of NDY laser rods.

4. Lasing Efficiencies of NDY Rods Containing 10 mole % ThO_2

The lasing efficiencies of several NDY rods with relatively low threshold values were measured and the results compared to that of glass:Nd. The influence of cooling cycle on lasing efficiency was also studied. In order to make a meaningful comparison of lasing efficiencies, the output energies experimentally determined were corrected for differences in surface area among the rods. The data were normalized with respect to the 0.25 inch diameter of the glass:Nd rod since it had the largest diameter and provided

an increased surface area available for capture of flashlamp radiation. The geometry of the pump cavity used in these tests was of the close-coupled-type which does not produce a well defined image of the pump lamp at the laser rod position. The total amount of pump energy absorbed by the rod is, therefore, dependent on the rod diameter and must be taken into consideration when comparing the efficiencies of rods of different diameters. The normalized data are given in Fig. 35 and the lasing efficiencies are listed in Table V.

TABLE V
LASING EFFICIENCIES FOR NDY AND LASER GLASS RODS

Sample	Efficiency (%) at 40 J Input Energy
12-1	0.04
12-1A	0.06
13-4	0.04
13-4A	0.12
27-4	0.14
OI, ED2 Glass	0.34

The importance of using a rapid cooling schedule for NDY rods is evident by noting that a 300% increase in lasing efficiency was obtained for 13-4A rod when compared to that found for 13-4 rod. The improvement in lasing efficiency of 12-1A over 12-1 rod is, again, not as large as 13-4A over 13-4 rod. It is not clearly understood why the rapid cooling procedure has not produced approximately equal improvements in optical quality in both 12-1A and 13-4A rods but slight differences in impurity levels and cooling rates

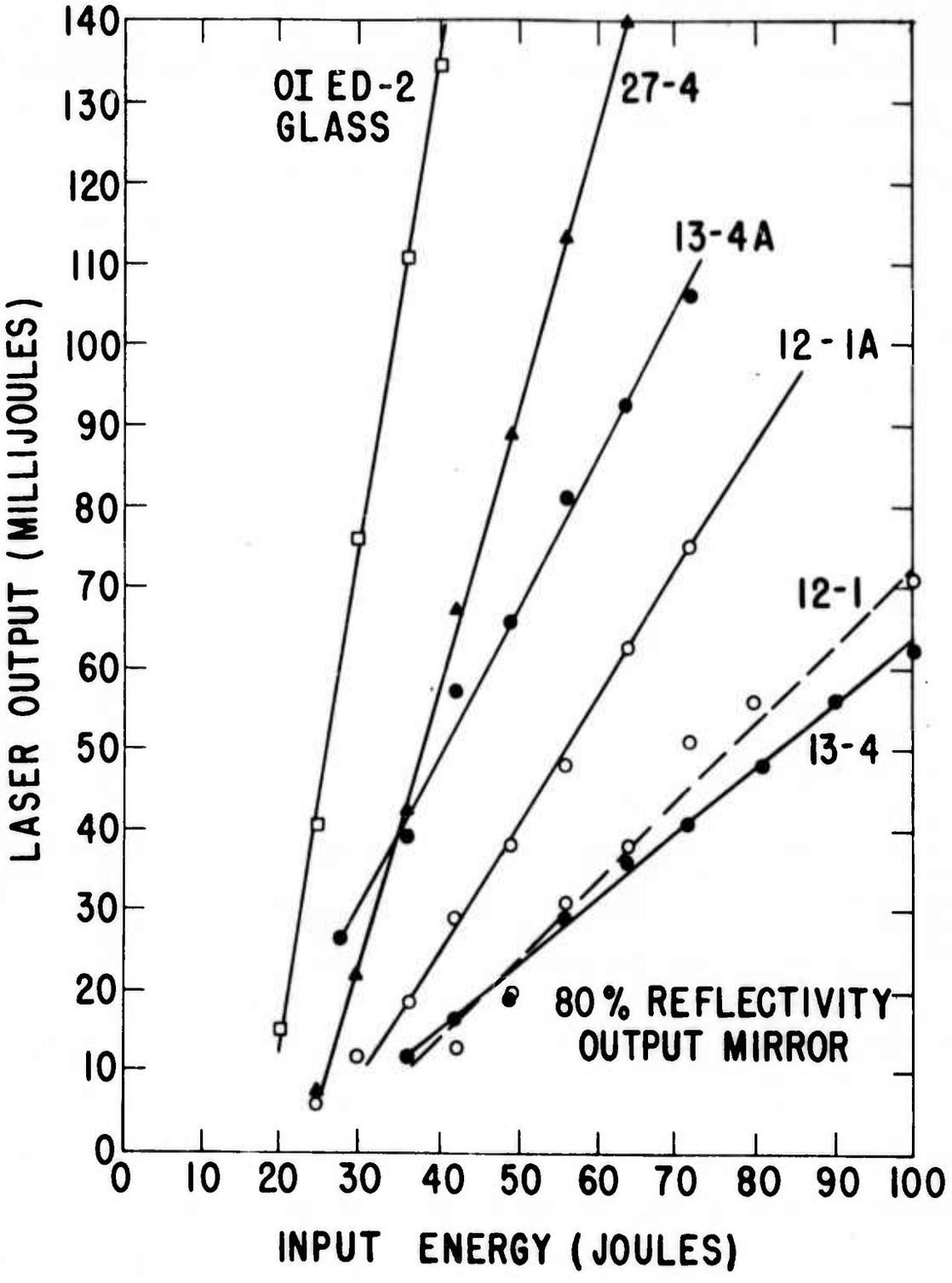

Figure 35 Laser output energy versus input energy for NDY laser rods, containing 10 mole % ThO_2, cooled slowly and rapidly from the sintering temperature of 2170°C. Owens Illinois ED-2 laser glass was used as a standard for comparison.

for these specimens may play an important role in forming ion clusters in the solid solution matrix during cooling.

The influence of powder preparation on lasing behavior has already been mentioned as being very important. Rod 27-4, which gave the highest output energy of all of the NDY rods containing 10 mole % ThO_2 in solid solution, was prepared from a starting oxalate powder derived by dripping a hot (85°C) Y-Th-Nd nitrate solution into a cold (5°C) oxalic acid solution. It is believed that this modification of the oxalate process gives rise to a high flux of ionic complexes of Nd, Y and Th which move to the nitrate droplet/oxalic acid solution interface and to a retardation of particle growth in the resulting liquid medium at low temperature. The output energy obtained from 27-4 rod is about 140 millijoules at an input energy of 64 joules. The lasing efficiency is about 41% that of best commercially available glass laser rod at 40J of input energy. For the sake of completeness, the laser threshold and active attenuation coefficient for 27-4 rod are 11 J and 2.4% cm^{-1}, respectively, and are listed in Table VI. In comparison to laser glass examined under identical experimental conditions, the threshold energy is slightly higher and the optical loss is about 3 times higher.

5. Influence of Composition on Lasing Behavior

Orange peel and extended defect formation are believed to be the primary causes of light scattering in NDY ceramics containing 10 mole % ThO_2 in solid solution. Both of these phenomena are directly related to the high ThO_2 content. The higher the ThO_2 content, the greater is the probability for compositional variations in the starting powder and, subsequently, in the final sintered product. Likewise, a high ThO_2 solubility in Y_2O_3 causes a large deviation from stoichiometry and promotes ion and defect clustering which give rise to extended defect formation during cooling. Therefore, the influence of re-

duced ThO_2 content on the optical quality of NDY ceramic was investigated.

The compositions investigated were 2.5 and 5 mole % ThO_2, with the Nd_2O_3 content fixed at 1 mole %. Powder preparation, processing, and heat treatment procedures used in preparing rod-shape specimens were similar to those used to prepare 27-4 rod, i.e. dripping hot nitrate into cold oxalic acid, ball milling step, soak time (~75 hrs) and rapid cooling cycle. Microstructural examination of polished sections of NDY ceramic containing 2.5 mole % ThO_2 in solid solution showed a classical case of discontinuous grain growth in which millimeter size grains are growing in a much smaller (~200 μm) average grain size matrix which contains a porosity ~5×10^{-6}. Laser rods could be synthesized with this composition, but their low fracture strength prevented mechanical finishing of these rods for laser testing. On the other hand, NDY rods composed of 5 mole % ThO_2 in solid solution could be synthesized and finished successfully for proper laser dimensions. Microstructural examination of sintered specimens of this composition reveals that the grain structure is very uniform and equiaxed and that the residual porosity is about 10^{-6} for specimens of good optical quality.

A high performance laser rod having a 5 mole % ThO_2 content is shown in Table VI and Fig. 36 and labeled 31-7. It has a lower threshold energy and about the same attenuation coefficient as those of 27-4 rod but has a lasing efficiency which is about 80% higher than that of 27-4. Since the attenuation coefficients are nearly the same, the increased output of 31-7 rod relative to 27-4 rod is caused by a higher gain coefficient associated with lower amounts of ThO_2 dissolved in the Y_2O_3 lattice. That is, the gain coefficient is inversely proportional to the fluorescent linewidth which is directly proportional to the ThO_2 concentration. By decreasing the ThO_2 content from 10 to

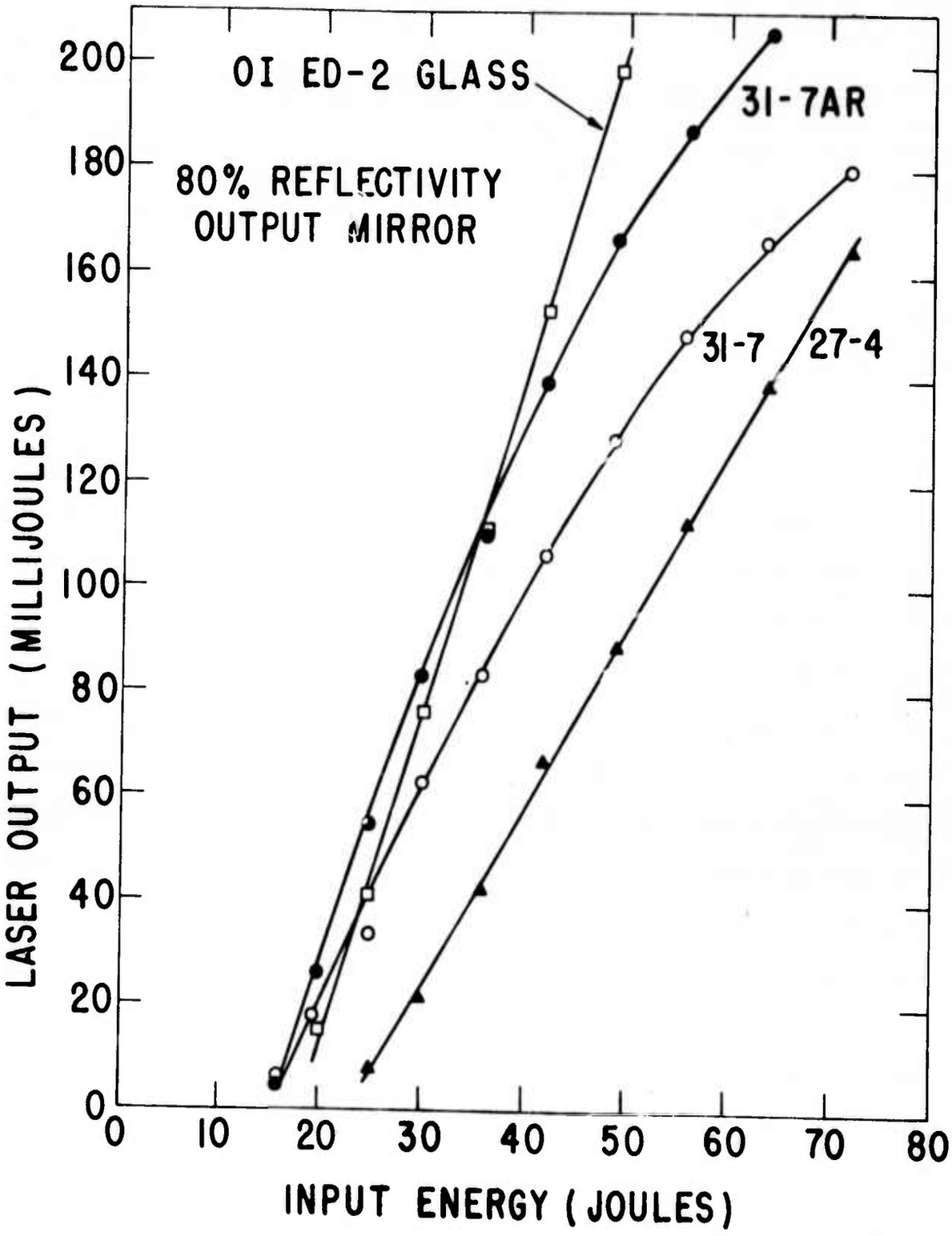

Figure 36 Laser output energy versus input energy for high performance NDY rods compared to a Nd:glass rod. AR = antireflection coated.

TABLE VI

LASER MEASUREMENTS FOR NDY RODS RELATIVE TO LASER GLASS

Specimen	ThO_2 Content	Laser Threshold (J) at 95% R2	Attenuation Coefficient	Lasing Eff. (%) at 40J Input Energy
27-4	10 Mole %	11	2.4% cm^{-1}	0.14
31-7	5 Mole %	8.2	2.3% cm^{-1}	0.25
31-7AR	5 Mole %	7.8	2% cm^{-1}	0.32
OI ED-2 Glass	—	9	0.76% cm^{-1}	0.34

to 5 mole %, the fluorescent linewidth decreases from 33 to 22 Å (see Fig. 33). It is assumed in the above interpretation that the refractive index and radiative lifetime are not drastically decreased by the reduction of ThO_2 content from 10 to 5 mole % in NDY ceramics.

The effect of rod end losses on the lasing performance of NDY rods is illustrated by the rod designated 31-7AR, where AR means antireflection coating. Rod 31-7 AR is the same rod as 31-7 except that it has MgF_2 antireflection coatings on both ends. Table VI shows that for 31-7AR rod the laser threshold and attenuation coefficient are lower, and the efficiency is higher than the corresponding values measured for 31-7 rod under identical experimental conditions. In the absence of an AR coating, about a 0.3% cm^{-1} optical loss is attributed to rod end effects. Hence, the intrinsic material loss coefficient for 31-7AR rod is indeed 2% cm^{-1}. The lasing efficiency at 40J of input energy is 0.32% for 31-7AR rod, which is 94% that of a laser glass rod (OI ED-2). By the application of an AR coating to 31-7 rod, the lasing efficiency is increased from 0.25 to 0.32%, which represents an increase of about 28%.

The nonlinear shape of the laser output curves found for 31-7 and 31-7AR rods, shown in Fig. 36, is believed to be related to amplified scattered radiation at high energy densities or output energies greater than about 100 mJ

for an output mirror reflectivity of 80%. The high scattering coefficients of about 1.6% cm^{-1} found in these NDY laser rods permit the amplification of scattered radiation confined within the laser rod and, as a result, extract energy from the main beam by depleting the population inversion of electrons. The intensity of scattered radiation will increase with increasing output energy and with increasing gain coefficient, which explains the decreasing slope of the output/input curves at higher input energies for NDY rods containing 5 mole % ThO_2 and explains why NDY rods containing 10 mole % ThO_2, such as specimen 27-4, do not exhibit this power loss because of its lower gain coefficient.

Laser rod 31-7AR gave the highest efficiency of any Nd-doped Yttralox rod tested. Below 35J of input energy, this rod produces more output energy than the best laser glass rod commercially available (see Fig. 36). In order to determine the maximum energy which can be delivered in the pulsed mode of operation from 31-7AR rod, the flash lamp intensity was increased to over 100 joules. For the pump cavity design employed, the 31-7AR rod 0.18 inches in diameter delivered 0.34J and 0.41J of optical energy at input energies of 112 and 162J, respectively, using a pump pulse of 150 μsec, and a 70% output mirror reflectivity. If these output energies are normalized for a rod 0.25 inches in diameter, then 0.47 and 0.57J of laser energy can be produced under identical conditions.

A periodical check of the calorimeter used for measuring output energy showed that the calorimeter was detecting only 70% of the true energy. Hence, all data points representing output energies should be multiplied by 1.4 The "corrected" maximum laser output delivered by 31-7AR rod, normalized to 0.25 inches in diameter, is 0.8J.

F. Laser Induced Damage Threshold

Many laser applications require operation at high power levels and high efficiencies. Under these severe conditions the laser host should have a relatively high damage threshold. The two most dominant damage mechanisms in inclusion-free crystalline and glass laser hosts are damage in the surface and in the bulk material. Both surface and bulk damage have been shown to be caused primarily by electron avalanche breakdown which results in plasma formation at the dielectric surface or within the laser host, respectively[28]. These damage thresholds depend on power density for nanosecond pulses and on energy density for picosecond pulses. In general, the surface damage threshold is about a factor of 4 or 5 lower than the intrinsic bulk damage threshold for the same material. Commercial laser glasses currently produced exhibit surface and bulk damage thresholds which are as high as 100 J/cm^2 and 400 J/cm^2 respectively, in Q-switched pulses[28].

In this section preliminary results concerning some of the gross physical characteristics of surface and bulk damage in Nd-doped Yttralox laser rods will be presented. In addition, the damage thresholds measured under active and passive conditions will be discussed. All damage measurements were obtained on NDY rods having a ThO_2 content of 10 mole %; rods with lower ThO_2 contents and higher optical quality were synthesized too late in this program for laser induced damage measurements.

1. Active Measurements

The NDY rod to be tested was assembled into stainless steel rod collets using "UHU-PLUS" epoxy. In order to prevent solarization, a yellow filter (Schott-OG530) was then cemented over the rod using RTV-102.

The rod assembly was then fixed in a tight pump cavity configuration in order to achieve increased pump lamp coupling efficiency. The pump cavity consisted of two Lexan End Caps which served as an interface between the pump cavity and water cooling system and as a mechanical support for the "DEWAR" type reflecting cavity which is elliptically shaped (0.8" x 0.7") and silver coated. An E. G. & G. Xenon Flash Lamp was employed in these experiments.

The optical configuration used for Q-switch testing is a typical variable output coupling cavity and is shown in Fig. 37. All elements are mounted on an optical bench with vernier adjustments in the X-Y planes. In addition, both mirrors are assembled into "Lansing" mirror mounts which provide fine adjustments for allignment. A He-Ne laser is used as an allignment standard.

The highest optical quality NDY rods selected for the Q-switching experiments were 27-4 and 12-1 rods. After repeated shots at 70 to 80 J of input energy some discoloration was observed in rods despite the presence of the filter. Upon removal of the collets cemented to a rod by a heat treatment process at 400°F for 4 hrs., it was observed that the discoloration or solarization had essentially disappeared. As a precautionary step these rods were completely desolarized by heat treating at 900°C for 4 hrs. in wet H_2. Q-switching tests were then conducted with a new filtering scheme which prevented light leakage between the filter and the cavity wall. Slight discoloration became noticeable only after the accumulation of many shots by using a repetition rate of 0.5 pps. It appears that discoloration is a function of the number of shots at high flash lamp intensities because discoloration never appeared in the earlier pulsed mode testing where the total number of shots were kept to a minimum.

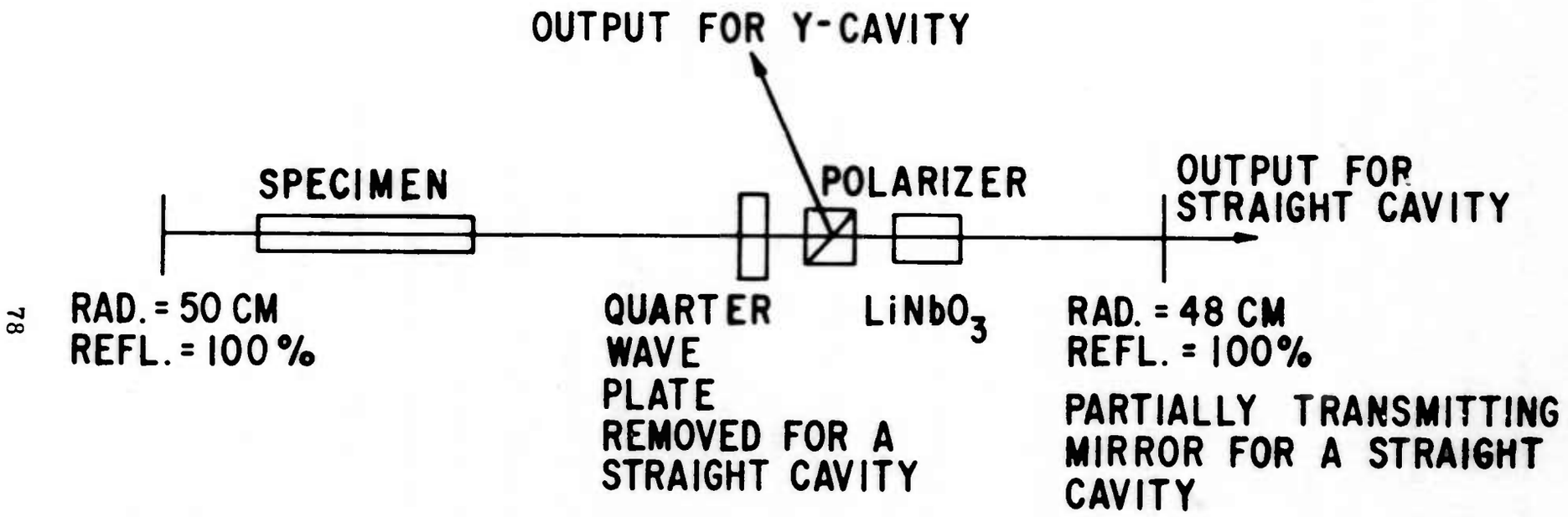

Figure 37 Optical schematic of Q-switching apparatus.

It was decided that the most representative value for damage threshold obtained under multimode condition would be that which just causes single-shot damage sites. For the 12-1 NDY laser rod with uncoated ends, surface damage occured when 17 mJ of output energy was obtained through a cross-sectional area of $3.73 \times 10^{-2} cm^2$ for a 35 nanosecond pulse and an 80% output mirror. This surface damage threshold is equivalent to an output power density of 13 MW/cm^2 or a peak internal power density of about 100 MW/cm^2, which was calculated by taking into consideration the high optical loss (~2% cm^{-1}) of the active medium. It was also observed that the $LiNbO_3$ crystal had surface damage at this light intensity. Although the power level for surface damage was obtained using a multimode beam, a higher surface damage threshold may be attained for a single mode beam and for a rod with antireflection coated ends. The damage threshold for 27-4 rod, which had higher optical quality and pulsed mode efficiency than 12-1 rod, was, unfortunately, not measured because this rod was fractured during preliminary experimental set-up.

Typical photomicrographs of surface damage sites on the faces of 12-1 rod are shown in Figs. 38 and 39. The average diameter and depth of a damage crater are about 60 μm and 15 μm, respectively. Each rod face contained about 75 damage sites. The surface of a crater or pit appears to be rough at the periphery but somewhat smooth in the center. The SEM photomicrographs in Fig. 39 lucidly reveal not only those general features of the damage crater already discussed but also show micropore and crazing formation. These qualitative features suggest that dynamic conditions similar to those necessary to form volcanic ash are attained at the rod surfaces when irradiated at high field intensities. That is, there appears

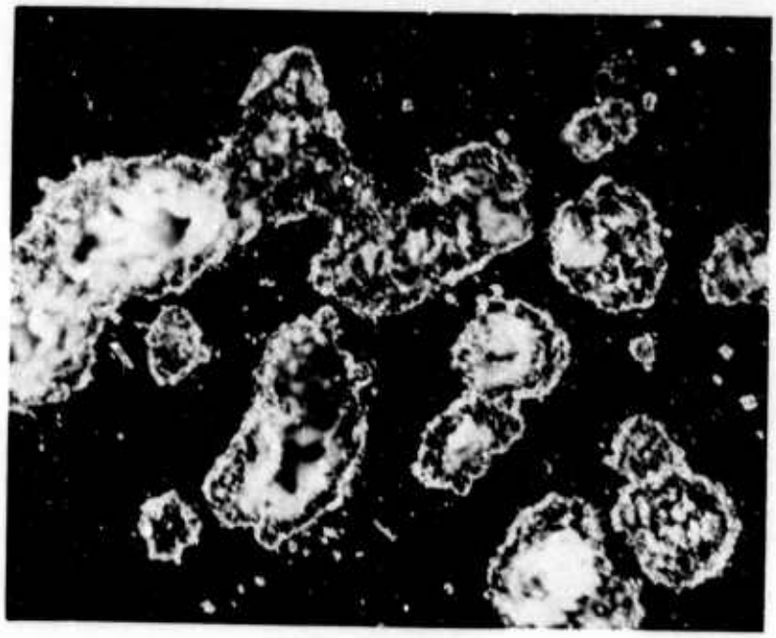

Figure 38 Surface damage sites on a Q-switched NDY laser rod (12-1). Dark field illumination. 200X

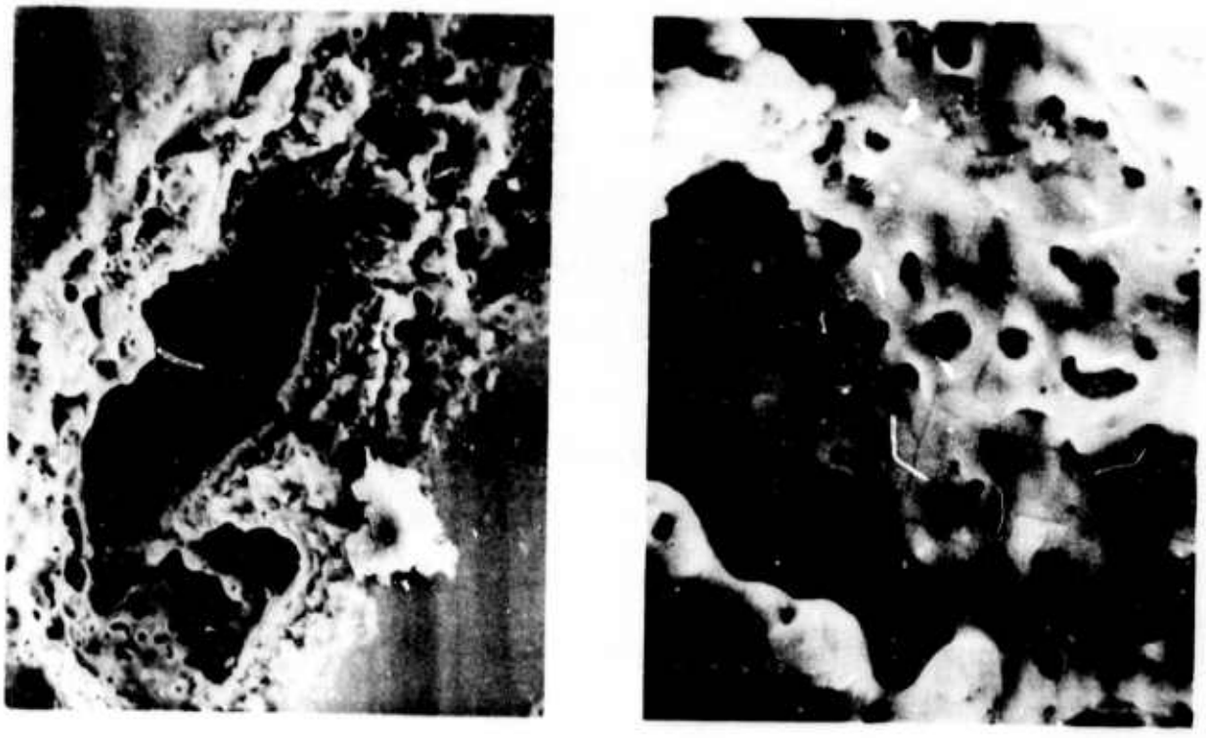

(a) 644X (b) 2300X

Figure 39 SEM photomicrographs of a typical surface damage site on 12-1 rod.

to be evidence that thermally-induced stresses (crazing), melting (smooth surfaces inside the crater) and violent plasma activity (micropore formation) have taken place at surface damage sites.

The rod faces were chemically etched to reveal the location of damage sites with respect to the grain boundaries. Examination of a large number of damage sites showed that damaged sites were located not only on grain boundaries but also entirely within the grain. This indicated that surface damage is not directly associated with the presence of grain boundaries in this isotropic material.

Preliminary microscopic investigations did not reveal any evidence of bulk damage in Nd-doped Yttralox ceramic tested under active conditions. This finding signifies that internal pores and grain boundaries are not presently limiting the damage threshold.

2. Passive Measurements

Bulk and surface damage thresholds were meausred and an assessment of the nature of the damage was made. These laser induced damage studies were performed under the direction of A. Feldman at the National Bureau of Standards, Gaithersburg, Md.

One laser rod, which was not antireflection coated and had an optical quality similar to 27-4 laser rod, was tested for laser damage by placing the rod in a focused laser beam generated by a Nd:glass laser operated in a well-controlled TEM_{oo} mode. The beam energy from this oscillator was about 80.5 mJ and varied by only $\pm$ 1/2% during the duration of the damage testing. For bulk damage the NDY rod was placed in the beam so that the front face was 12.7 mm in front of the focus. Because NDY

ceramic has a refractive index of 1.89 at 1.064 μm, the focus in the rod was about 24 mm from the entrance face. The damage threshold was determined by accepting the lowest power levels which produced visible plasma formation. The general procedure was to fire the laser, operated at about 85 mJ of output energy, at about 5 min. intervals, vary the transmission filters which were placed in the beam path in front of the test sample, and detect a visible plasma by direct observation and by photography.

The bulk damage threshold of a NDY laser rod in comparison to several glasses and YAG single crystal is listed in Table VII. Since the exact beam diameter at the focal plane is not exactly known but predicted to be 29.4 μm absolute values

TABLE VII

RELATIVE BULK DAMAGE THRESHOLDS

25ns PULSE WIDTH

181mm FOCUSING LENS

Specimen	Pulse Energy (mJ)	Peak Pulse Power (MW)
BSC 517	22	.75
Dense Flint SF55	3.74	.128
Fused Silica	29.2	1.00
YAG	11	.36
NDY Ceramic	5.47	.187

of damage threshold are given in terms of pulse energy and peak pulse power rather than in power density. These damage thresholds are calculated by taking into account the reflection losses due to the focussing lens and the sample surface, and the total transmission of the filters. NDY

ceramic has a damage threshold that is higher than that of dense flint glass but only 1/4 that of a borosilicate crown glass and about 1/2 that of YAG single crystal.

The surface damage threshold was also measured for NDY ceramic by using the same experimental techniques except that the sample surface was located at the focal plane. Results of this investigation showed that the pulse energy and peak pulse power at the damage threshold were 1.5 mJ and 0.051 MW, respectively. The bulk damage threshold for NDY ceramic is about 4 times higher than the surface damage threshold, a ratio which is in accord with damage results found for sapphire and laser glass[29]. It has been recently proposed[29] that there is an electric field enhancement near surface pores, scratches and microcracks which can account for the lower apparent threshold intensity for surface damage.

The gross general features of bulk damage are illustrated in Fig. 40. An end view of a bulk damage site in transmitted white light shows that there are fracture surfaces radiating outward from the central region of the damage site. Grain boundaries probably account for the changes in direction of propagation of a single radiating microcrack. A view of the same damage site in crossed nicols (Fig. 40 b) reveals that strain induced birefringence is associated with the damage site and that the highest strain is observed to be in the immediate vacinity of the damage site. Strain effects are observed as much as 1 mm away from the central damage spot. Note also that individual grains can be observed in the residual stress field.

The qualitative features of a surface damage site is illustrated in Fig. 41. Damage appears to have occurred in the vacinity of a 3-grain intersection. The orientation of the microcracks is different in each grain but this observation is not obvious because during specimen

(a) 50X

(b) 37X

Figure 40 End view of bulk damage site. (A) Transmitted light; (B) Crossed nichols.

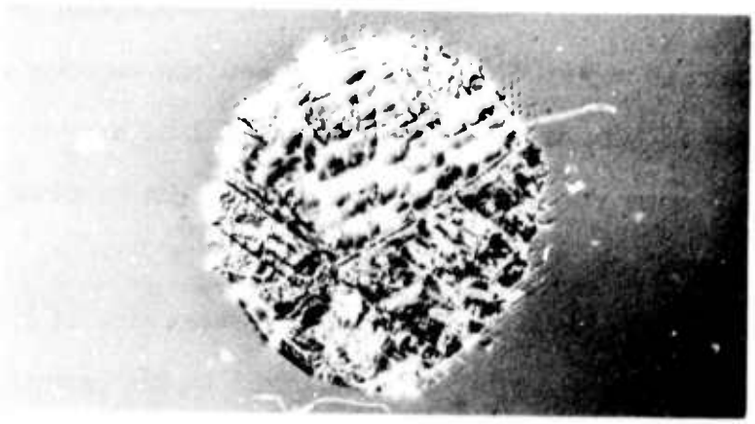

Figure 41 Surface damage site on a NDY laser rod under passive testing. Reflected light, dark field illumination. 518X

cleaning before photographing there was spalling or flaking of the surface material. A development of a mesh of fine cracks can also be observed along the circumference of the damage site which lead into the undamaged material. Finally note that the surface finish is not of the best quality since many surface scratches are visible at 750X.

In summary, it should be emphasized that all damage measurement were made on NDY rods of good optical quality but not of the best quality. Furthermore, none of the rods analyzed for damage threshold were anti-reflection coated for $\lambda = 1.064$ μm. Finally, no major precautions were taken to understand the effect of surface polish and cleanliness on the surface damage threshold. Therefore, it is believed that one can expect a higher surface damage threshold of NDY laser rods by taking into account the above important considerations.

VII. REFERENCES

1. E. C. Subarrao, P. H. Sutter and J. Hrizo, "Defect Structure and Electrical Conductivity of ThO_2-Y_2O_3 Solid Solutions," J. Am. Ceram. Soc., 48 (9) 443-46 (1965).
2. P. J. Jorgensen and R. C. Anderson, "Grain-Boundary Segregation and Final-Stage Sintering of Y_2O_3," ibid, 50 (11) 553-58 (1967).
3. Eastman Kodak Co., Publication No. U-72, 1971.
4. G. H. Haertling, "Improved Hot-Pressed Electrooptic Ceramics in the (Pb, La) (Zr, Ti) O_3 System," J. Am. Ceram. Soc., 54 (6) 303-09 (1971).
5. J. E. Genic, H. M. Marcos and L. G. Van Uitert, "Laser Oscillations in Nd-Doped Yttrium Aluminum, Yttrium Gallium, and Gadolinium Garnets," Appl. Phys. Letters, 4 (10) 182-84 (1964).
6. J. D. Myers, "Glass Laser Materials," p.3, Owens-Illinois, Inc. (1972).
7. J. R. Thornton, W. D. Fountain, G. W. Flint, and T. G. Crow, "Properties of Neodymium Laser Material," Appl. Opt., 8 (6) 1087-1102 (1969).
8. C. Greskovich and K. N. Woods, "Fabrication of Transparent ThO_2-Doped Y_2O_3," J. Am. Ceram. Soc., 52 (5) 473-78 (1973).
9. S. Prochazka and R. L. Coble, "Surface Diffusion in the Initial Sintering of a Alumina. I. Model Considerations," Phys. Sintering 2 (1) 1-18 (1970).
10. W. D. Kingery and B. Francois, "Grain Growth in Porous Compacts," J. Am. Ceram. Soc., 48 (10) 546-47 (1965).
11. D. Kellam and P. S. Nicholson, "Pore Shape Changes During the Initial Stages of Sintering," ibid. 54 (2) 127-28 (1970).
12. J. J. Sipe and O. J. Whitemore, Jr., "Pore Growth During Initial Stages of Sintering," Bull. Am. Ceram. Soc. (Abstract 62-B-71), 50 (4) 376 (1971).
13. R. J. Brook, "The Impurity-Drag Effect and Grain Growth Kinetics," Scripta Met., 2 375-78 (1968).
14. I. M. Lifshits and V. V. Slezov, "Kinetics of Diffusive Decomposition of Supersaturated Solid Solutions," Soviet Physics JETP (English Transl.), 35 (8) 331-39 (1959).

15. R. L. Coble, "Sintering Crystalline Solids.I," J. Appl. Phys., 32 (5) 787-92 (1961).
16. F. Thummler and W. Thoma, "The Sintering Process," Met. Reviews, 1 69-108 (1967).
17. J. H. Rosolowski and C. Greskovich, "Analysis of Pore Shrinkage By Volume Diffusion During Final Stage Sintering," J. Appl. Phys., 44 (4) 1441-50 (1973).
18. D. L. Johnson, Sintering and Related Phenomena, Conference Proceedings, Notre Dame U., June 1965, Gordon and Breach, New York, N. Y. (1967).
19. D. L. Johnson, "A General Model for the Intermediate Stage of Sintering," J. Am. Ceram. Soc., 53 (10) 574-77 (1970).
20. H. U. Anderson, "Initial Sintering of $BaTiO_3$ Compacts," ibid., 48 (3) 113-21 (1965).
21. A. F. Wells, Structural Inorganic Chemistry, 3rd Edit., Oxford University Press, Ely House, London (1962).
22. E. Snitzer, "Glass Lasers," Appl. Optics, 5 (10) 1487-99 (1966).
23. T. C. Rich and D. A. Pinnow, "Total Optical Attenuation in Bulk Fused Silica," Appl. Phys. Lett., 20 (7) 264-66 (1972).
24. D. Ross, Lasers, Light Amplifiers, and Oscillators, Adademic Press, Inc., New York, p.143 (1969).
25. Van De Hulst, Light Scattering By Small Particles, John Wiley and Sons, Inc., New York, pp.64 and 107 (1957).
26. C. P. Schillaber, Photomicrography in Theory and Practice, John Wiley and Sons, Inc., New York, p. 471 (1947).
27. Richard D. Brew Co., Inc., Concord, New Hampshire.
28. A. J. Glass and A. H. Guenther, "Laser Induced Damage of Optical Elements - a Status Report," Appl. Opt., 12 (4) 637-49 (1973).
29. N. Bloembergen, "Role of Cracks, Pores, and Absorbing Inclusions on Laser Induced Damage Threshold at Surfaces of Transparent Dielectrics," Appl. Opt., 12 (4) 661-64 (1973).